Optical fibre-based minimally-invasive blood glucose monitoring system.

VISWAMBARAN, V.

2018

Optical Fibre based Minimally-Invasive Blood Glucose Monitoring System

Vivek Viswambaran

MRes *2018*

Optical Fibre based Minimally-Invasive Blood Glucose Monitoring System

Vivek Viswambaran (1219052)

A thesis submitted in partial fulfilment of the requirement of the

Robert Gordon University

for the degree of Master of Research

This research programme was carried out in collaboration with

University of Aberdeen

October 2018

Principal Supervisor: Dr. Radhakrishna Prabhu

Abstract

Obesity and changing lifestyle have made diabetes mellitus as one of the world's foremost metabolic syndrome and thus affecting the lives of around 380 million people around the globe. Although considered incurable, adverse effects of diabetes can be controlled by tight monitoring of blood glucose levels. Over the years several methods have been proposed for the same.

A thorough literature and patent review were conducted and it was realised the blood glucose monitors (BGMs) based on amperometry are amongst the most widely developed technology for blood glucose monitoring. However, these sensors are invasive in nature and have bio-compatibility issues. Also, the electrochemical sensors are not stable due to the electroactivity of other blood constituents and thus requiring frequent calibrations, hence the need for an alternate approach.

In this work, it has been shown that optical fibre can act both as a sensing element and a medium to carry information in real time. Optical methods are useful as they require a very small sample volume (< 1 μL) and are also capable of remote probing.

An investigation into various microstructured optical fibres has also been conducted and analysed mathematically. This led to proposing an integration of microstructured optical fibre and associated techniques. Boronic acid-based glucose sensing moiety has been selected due to its high affinity for glucose and its ability to decouple from glucose making it a good contender for continuous or reusable blood glucose sensor. Preliminary investigation has concluded that 4-vinylphenylboronic acid (VPBA) can be incorporated into

poly(methylmethacrylate) (PMMA) matrix without losing its ability to bond with glucose. Further, fabrication of VPBA and Rhodamine-6G (Rh-6G) doped optical fibre ring resonator has been successful and that performance has been analysed mathematically. Rh-6G has retained its fluorescence properties even after doping with PMMA & VPBA and fibre drawing process which can be helpful to create microresonator with the lasing gain medium. The study can be taken forward and in future be extended to *in vitro* and *in vivo* studies with blood or blood substitute.

Keywords: Blood Glucose Sensor (BGM), Fibre Optic Sensor, Optical Micro Resonator, Boronic Acid Based Glucose Sensor, PMMA Micro Resonator.

Acknowledgement

I wish to offer my thanks to the following people who have influenced, guided and contributed towards this research project. Firstly, to the supervisory team, Dr Radhakrishna Prabhu (RGU), Dr Simon Officer (RGU) & Dr Nakkeeran Kaliyaperumal from University of Aberdeen. They have been instrumental in guiding me throughout my research work and enabling me to complete the thesis. Special thanks also go to Mr Jaison Peter, Mr Linslal, Dr M. Kailas & Prof P. Radhakrishnan for all their help and advice with the fabrication of Hollow core fibre and with various other experiments carried out at International School of Photonics, CUSAT, India during UGC-UKIERI project. I would also like to thank all the technician staff who helped me throughout my work including Iain Tough and Emily Hunter for carrying out the SEM analysis. Further thanks also go to Kaushal Bhavsar for his advice and friendship for the past four years and to my parents, my wife for putting up with me during my writing up period.

Table of Contents

Table of Figures

List of Acronyms

ADP	*Adenosine Diphosphate*
ATP	*Adenosine Triphosphate*
BF	*Bare Optical Fibre*
BGM	*Blood Glucose Monitors*
BPO	*Benzoyl Peroxide*
CGM	*Continuous Glucose Monitoring*
ConA	*Concanavalin A*
EDG	*Electron Donating Group*
EWG	*Electron Withdrawing Group*
FAD	*Flavin Adenine Dinucleotide*
FADH2	*Flavin Adenine Dinucleotide, reduced*
G6P	*Glucose-6-Phosphate*
G6PD	*Glucose-6-Phosphate Dehydrogenase*
GDH	*Glucose Dehydrogenase*
GOD	*Glucose oxidase*
HC	*POF- Hollow Core Polymer Optical Fibre*
HCF	*Hard Clad Optical Fibre*
HEMA	*Hydroxyethylmethacrylate*
ITF	*Inverted Trench Optical Fibre*
LC-POF	*Liquid core Polymer Optical Fibre*
MMA	*Methylmethacrylate*
MMF	*Multimode Optical Fibre*
mPOF	*Microstructured Polymer Optical Fibre*
MSF	*Micro Structured Optical Fibre*
NADP	*Nicotinamide Adenine Diphosphate*

NADPH	*Nicotinamide Adenine Dinucleotide Phosphate-Oxidase*
NIR	*Near Infrared*
OCT	*Optical Coherence Tomography*
OFRR	*Optofluidic Ring Resonator*
PBG	*Photonic Band Gap*
pKa	*Acid Dissociation Constant (Logarithmic)*
PML	*Perfectly Matched Layer*
PMMA	*Poly(methylmethacrylate)*
POF	*Polymer Optical Fibre*
PQQ	*Pyrroloquinoline Quinone*
Rh-6G	*Rhodamine-6G*
rpm	*Rotation Per Minute*
SEM	*Scanning Electron Microscope*
TIR	*Total Internal Reflection*
UGC	*University Grants Commission*
UKIERI	*UK-India Education and Research Initiative*
UV	*Ultra Violet*
VPBA	*4-Vinylphenylboronic Acid*
WGM	*Whispering Gallery Mode*

List of Symbols

ψ_z	Amplitude of the axial magnetic (TE) or electrical (TM) modal field
μ_s	Scattering coefficient
α	Absorption coefficient
ρ	Fibre core radius
V	Normalized frequency
f	Fraction of power located in the liquid filled hole
D	Preform diameter
d	Fibre diameter
µL	Microlitres
Er	Radial electrical field intensity
I	Reflected light intensity
I_0	Incident light intensity
m	Azimuthal Quantization Number
mA	Milli Ampere
mg dL-1	Milligram per deciliter
mM	Millimolar
n	Refractive index of medium
N_{clad}	Number of air cells in cladding of holey fibre
N_{core}	Number of air cells in core of holey fibre
P_f	Packing fraction
Þ	Phase factor
v	Mode index
β	Propagation Coefficient
γ	Attenuation Coefficient
Δη	Delta change in power fraction

λ	Wavelength of electro-magnetic wave
λ_{ab}	Wavelength of Absorption
λ_{ex}	Wavelength of Excitation
μ_{eff}	Effective attenuation coefficient
μ_a	Absorption coefficient
θ_i	Incident ray angle
θ_c	Critical angle
θ_t	Transmitted ray angle
n_{eff}	Effective Refractive index of the propagating mode
k_t	Wave vector associated with transmitted wave
k_0	Wave vector in free space
E	Electric Field
d_p	Penetration depth
P	Total power in fibre
P_{clad}	Power in fibre cladding
V_{MSF}	Interaction volume in Microstructured optical fibre
V_{MMF}	Interaction volume in multimode optical fibre
V_{core}	Interaction volume in fibre core
V_{clad}	Interaction volume in fibre cladding
r	P ower fraction outside the fibre core
r_v	Evanescent power fraction in multimode fibre
Λ	Pitch
r_c	Cell radius
η	Evanescent power fraction in ψ direction
$L_c(\lambda)$	Confinement Loss
J_m	m th order cylindrical Bessel function

N_m	m th order cylindrical Neumann function
$H_m^{(1)}$	Hankel function of the first kind
v_{draw}	Fibre draw speed
$v_{preform}$	Preform feed rate

Chapter 1 - Introduction

Diabetes is a metabolic disorder characterised by chronic hyperglycemia together with an imbalance in carbohydrate, fat and protein metabolism [1]. Hyperglycemia is the increase of blood glucose level above the normal range (80-120 mg/dL) and can occur when the pancreas is not producing the hormone insulin or the body is unable to produce enough and/or has become insensitive to insulin.

According to the International Diabetic Foundation, diabetes is affecting the lives of over 382 million people around the globe; an additional 316 million people are at high risk with impaired glucose tolerance. It has been predicted that by 2035 these numbers are going to rise by 55% due to increase in population, ageing, lifestyle related issues and urbanization [2].

Recent studies suggest that the influence of diabetes is not only in the lives of people (premature deaths of around 5.1 million) but also on society by creating a financial and economic burden. To quote diabetes as ”a disease of wealthy” would be a misconception as more than 80% of cases are found in low and middle-income countries. In 2013 alone, a total of USD 548 billion has been spent as healthcare expenditure for diabetes. This is about 11.6% of the total global expenditure on all health care services [3], [4].

1.1 Classification of different types of diabetes

Diabetes can be classified into three groups; namely Type 1, Type 2 and Gestational diabetes.

Type 1 comprises of cases which are primarily due to the destruction of insulin-producing islet beta-cells in the pancreas and the body is prone to ketoacidosis. Destruction of beta-cells is a result of the auto-immune response of the body and the resulting condition is fatal. The patients solely depend on a regular dosage of insulin for survival. Fortunately, the number of Type 1 cases reported are significantly low, contributing to only 5-10% of the total [5]. Type 1 diabetes may affect people of any age but is prone to occur in children and teenagers [1].

Type 2 is the most common form of diabetes mellitus affecting over 90-95% of total diabetes patients around the globe [6]. This type of disorder arises due to the body's inability to secrete enough insulin or showing resistance to the same [1]. Since the symptoms of Type 2 diabetes can lay dormant for years in affected people, the diagnosis and subsequent treatment delays can lead to severe complications in the body.

Gestational Diabetes is the carbohydrate intolerance in pregnant woman resulting due to the hormonal changes that happen during the 24^{th} week of pregnancy. These hormonal changes are thus capable of blocking the action of insulin and hence resulting in diabetes [1]. This condition generally recedes towards the end of pregnancy [6] but can affect both mother and unborn child if left unattended. However, women with the history of gestational diabetes and the babies born to them are at a higher risk of developing obesity and Type 2 diabetes later in their life [7].

Figure 1-1 below represents a pictorial explanation for different types of diabetes.

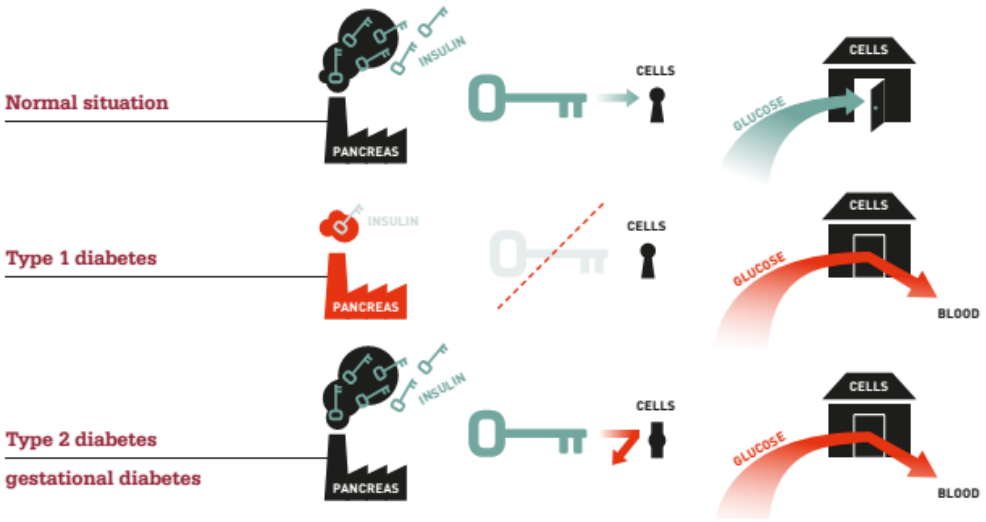

Figure 1-1: A simple representation of different classifications of diabetes

Source: International Diabetes Federation (http://www.idf.org/diabetesatlas)

1.2 Complications associated with diabetes

Health problems for diabetes patients are numerous, which include increased risks of heart diseases, kidney failure, losing sensitivity due to degrading nerve endings and blindness. Diabetic patients are also at high risk of incurring infections in flesh wounds which can lead to amputations and death [8].

Nearly 21% of Type 2 patients develop some form of eye disease by the time they have been diagnosed with diabetes. Diabetes can severely affect the carotid artery (macular oedema or capillary non-perfusion) and is capable of damaging the optic nerve and retina [9].

Hyperglycemia together with high blood pressure, cholesterol and obesity can lead to high risks of cardiovascular diseases. Cardiovascular diseases include

myocardial infarction (heart attack), stroke, peripheral artery disease, leading to heart failure [10].

Sustained hyperglycemia and high blood pressure can initiate neuron degradation leading to cardiac autonomic neuropathy, loss of sensitivity, motor neuron control, gastroparesis, sexual dysfunction, neurogenic bladder, myocardial infarction, malignant arrhythmia and sudden death [11]. In peripheral neuropathy, affected areas are extremities of limbs causing loss of sensation in the fingers and feet. This condition can be dangerous since injuries to these parts can go unnoticed leading to infection and amputation [8], [12].

Diabetic people are more prone to nephropathy (kidney disease) than those without. Albuminuria (presence of protein Albumin in urine) and Polyuria (frequent urination) are the main complications caused by diabetes which can overload the kidney and affect its normal functioning [13].

1.3 Need for blood glucose measurement for diagnosis & treatment of diabetes

In most cases, the clinical diagnosis of diabetes is done when patients resort to medical attention for the symptoms shown by the same.

Type 1 diabetes can be sudden and is characterised by Polyuria (frequent urination), Polydipsia (increased thirst), Polyphagia (increased hunger), Weight loss, blurred vision, poor wound healing (cuts, scrapes, etc.) dry mouth and dry or itchy skin. Most of these symptoms being evident can be diagnosed and subsequently controlled [5], [14].

Type 2 diabetes generally has symptoms including sweating, tachycardia, palpitations, nervousness, tremors, weakness, headache, mental confusion, fatigue etc. Symptoms in diabetic patients with Type 2 condition may take several years to appear [6], [8] and/or is often ignored resulting in delayed diagnosis. The delay can adversely affect the body due to hyperglycemia and subsequent complications.

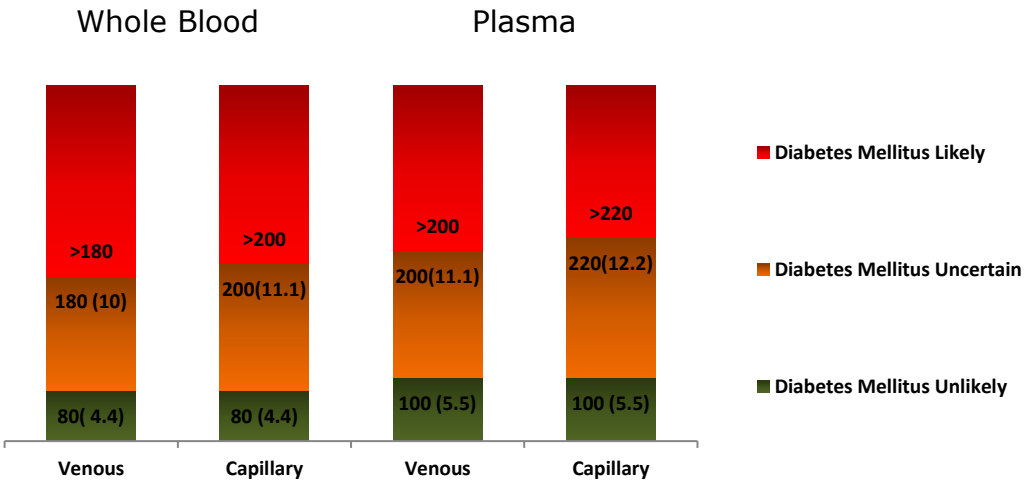

Figure 1-2: Casual/Random blood glucose values in mg dL^{-1} (mmol $^{-1}$). Red zone confirms the patient to be diabetic, while if in green means non- diabetic. The orange zone shows the glucose levels for which the diagnostics are uncertain.

Adapted from1985 WHO Study Group [15]

Figure 1-2 (above) shows blood glucose values for clinical diagnosis of diabetes mellitus. The figure shows how blood glucose threshold values depend on whether blood is taken from a vein or capillary and whether whole blood or plasma is used for glucose monitoring. A detailed analysis of blood and longer observation is required to draw any conclusions.

1.4 Literature and patent review

Serious complications of diabetes can be diagnosed and controlled by stringent personal monitoring of blood glucose level [16]. Blood glucose sensors can be broadly classified as Invasive, Minimally Invasive and Non-Invasive types based on how the analytical devices come in contact with a patient's body. Figure 1-3 shows a different classification of existing technology

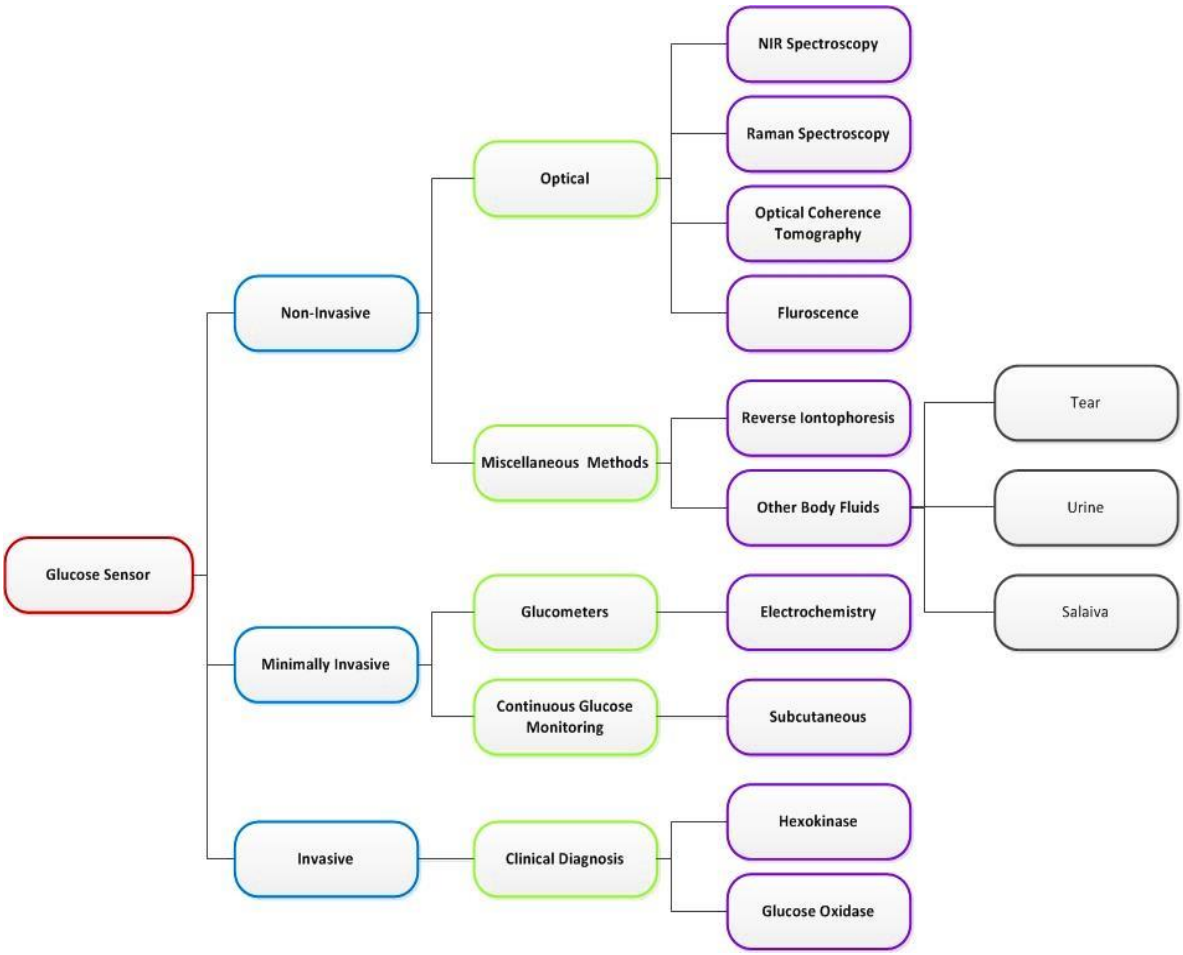

Figure 1-3: Classification of existing blood glucose monitoring methods

1.4.1 Invasive blood glucose monitoring techniques

Almost all clinical methods of glucose monitoring come under this classification. Invasive techniques involve puncturing the skin with a

hypodermic needle for accessing blood from a vein. Typical blood volumes in the order of several millilitres are collected as a sample. The most common glucose specific enzymes used are glucose oxidase and hexokinase. These enzymes together with an indicator are capable of measuring the glucose levels by monitoring the colour change by colourimeter or spectrophotometer. In order to avoid the reducing capabilities of other blood constituents, glucose measurement is conducted on plasma extracted from blood using a centrifuge [17], [18].

1.4.1.a) Glucose Oxidase Method

This is a two-step method. In the first step, glucose is converted to gluconic acid and hydrogen peroxide (H_2O_2) in the presence of oxygen and glucose oxidase as a reagent (shown in Equation 1 below). The gluconic acid and hydrogen peroxide so produced will be proportional to the glucose concentration. Hydrogen peroxide will then be converted to water (H_2O) in the presence of the co-enzyme peroxidase and in this process, the indicator will also be reduced to show a colour change.

$$\text{Glucose} + O_2 \xrightarrow[\text{Oxidase}]{\text{Glucose}} \text{Gluconic acid} + H_2O_2 \qquad (1)$$

$$H_2O_2 + \text{Indicator} \xrightarrow{\text{Peroxidase}} 2H_2O + \text{Colour formation /Change} \qquad (2)$$

The colour change will be proportional to the glucose concentration which can be measured by a colourimeter or spectrophotometer. The reaction is also oxygen dependent which can be a limiting factor for the same.

1.4.1.b) Hexokinase Method

This is also a two-step method and has more advantages than the glucose oxidase method as it is less affected by other blood constituents and uses safer reagents [18].

$$\text{Glucose} + \text{ATP} \xrightarrow{\text{Hexokinase}} \text{G6P} + \text{ADP} \quad (3)$$

$$\text{G6P} + \text{NADP} \xrightarrow{\text{G6PD}} \text{6PG} + \text{NADPH} \quad (4)$$

As a first step, glucose is converted to glucose-6-phosphate (G6P) in the presence of hexokinase and adenosine triphosphate (ATP). ATP is also reduced to adenosine diphosphate (ADP). In the second step in the presence of G6PD and G6P, nicotinamide adenine diphosphate (NADP) is converted to 6-phosphogluconate (6PG) and nicotinamide adenine dinucleotide phosphate-oxidase (NADPH). NADPH can absorb UV light at 340 nm. Glucose concentration can be directly correlated to the absorption spectra of NADPH using a spectrophotometer.

Even though accurate, due to the invasive nature, this method is not advisable for frequent measurements. It is also time consuming, inconvenient for patients and would require a qualified laboratory technician for the procedure.

1.4.2 Non-invasive blood glucose monitoring techniques

Measuring blood glucose levels remotely and being able to do it continuously would be an ultimate achievement in the field of glucose sensing. Non-invasive methods can eliminate various challenges like pain and discomfort of using

implantable sensors. A non-invasive method with sufficient accuracy is always preferred over other measurement techniques.

1.4.2.a) Optical transducers

Optical transducers may use variable frequencies of the electromagnetic spectrum to probe different material property remotely. This incorporated in the sensor may utilize various properties of light to interact with glucose molecules in a concentration-dependent manner. They may interact with blood through intervening tissues including skin, protein, lipids and bone. These sensors can either directly sense based on chemical properties of the glucose structure or indirectly by measuring the effects of blood glucose level on body temperature, pH or impedance [19]. Since it is an optical signal, it remains unaffected by electromagnetic interferences.

i) Near Infrared Spectroscopy

Near-infrared (NIR) utilizes light between 0.7-1.4 μm of the electromagnetic spectrum. Typical penetration depth ranges from 1-100 μm in the human body and decreases with increase in wavelength. Scattering and absorption are the major phenomena encountered by light when focused on the body. Light propagation is characterised by the light transport theory as given below [20].

$$\mathrm{I} = I_0 \, e^{-\mu_{eff} \cdot d} \qquad (5)$$

where,

I = Reflected light intensity

I_0 = Incident light intensity

μ_{eff} = Effective attenuation coefficient

d = Optical path length in tissue

Effective attenuation coefficient can also be expressed as a function of absorption and scattering coefficient since light is partially absorbed and also scattered by the issue.

$$\mu_{eff} = f(\mu_a, \mu_s) \quad (6)$$

where,

μ_a = Absorption coefficient

μ_s = Scattering coefficient

NIR spectroscopy works on the principle of measuring the attenuation coefficient brought upon by the variation of blood glucose level in the tissue under observation.

Limitations include the large absorption band of water in tissue which overwhelms and also overlap the relatively small absorption coefficient of glucose. Not only that, the weak spectral signal from glucose is affected by water but also by haemoglobin, lipids and proteins in the tissue. Further, the signal is also affected by the physical and chemical parameters of the body (temperature, pressure, skin hydration and pigments). Also, these parameters change from one subject to another and provide an immense challenge in complex signal processing.

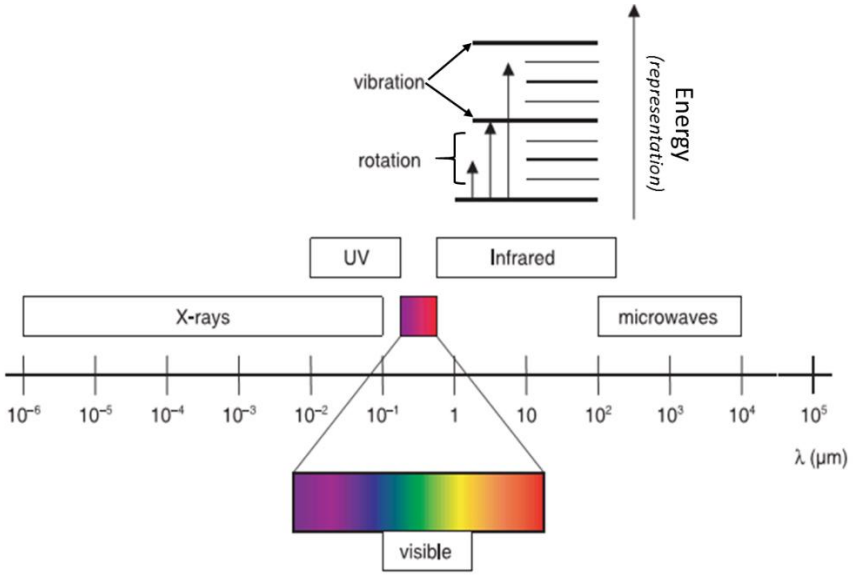

Figure 1-4: Electromagnetic spectrum

The figure shows the infrared wavelengths of light capable of inducing molecular rotation and vibration which can be used for sensing (adapted from [21])

ii) Raman Spectroscopy

Raman spectroscopy detects shifts in the wavelength of the inelastically scattered radiation that provides the chemical and structural information of materials being probed. Raman shifted signal can be of either higher energy or of lower energy as shown by anti-stokes and stokes line in Figure 1-5. Raman signature is a property of symmetric molecules and water being a low symmetry molecule has a very weak Raman signal which will not interfere with glucose measurement as in NIR spectroscopy. Due to the shift in Raman signal received, it is also easier to filter. Raman spectral peaks for glucose can be observed at 911, 1060 and 1125 cm^{-1} [22].

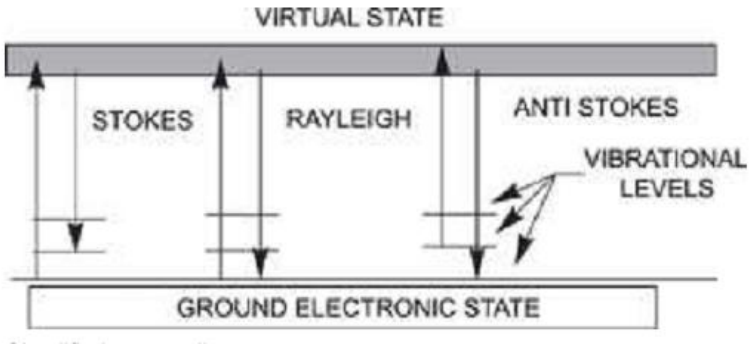

Figure 1-5: Simplified Energy Diagram.[23]

Even with these benefits the Raman signal is very weak compared to (10^{-3} times) the original signal and needs very powerful detector and long spectral acquisition time with respect to other optical methods [24].

iii) Optical Coherence Tomography (OCT)

Optical coherence tomography (OCT) is an interferometric method based on using light with low coherence length, such as a white light. Light in OCT is split into a reference arm and sample arm (a moving mirror). The reflected (backscattered) light from the tissue sample is then combined with the reference signal to produce an interference pattern but only if light from both hands have travelled the same distance. Thus scanning the mirror in the reference arm can enable OCT to scan up to a depth of 1 mm. Backscattered signal from the tissue is dependent on the refractive index of the interstitial fluid. Variation in interstitial glucose level will change the refractive index and hence the scattering coefficient which will be recorded in the interference pattern. The OCT pattern thus recorded can be used for blood glucose estimation.

OCT is sensitive to motion artefacts, temperature, tissue heterogeneity and interfering analytes [25].

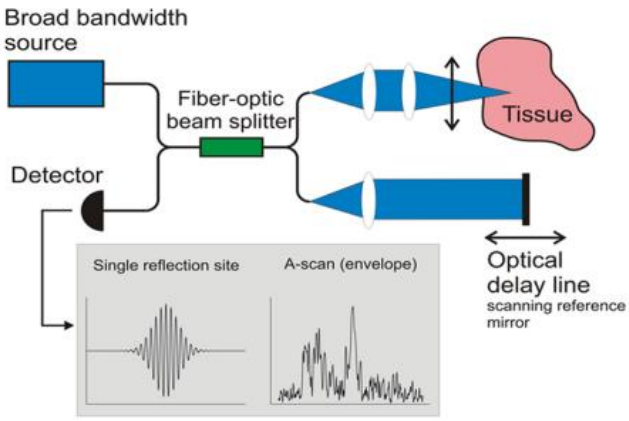

Figure 1-6: Schematic Diagram of OCT setup [26]

iv) Fluorescence

Fluorescent-based sensors depend on the fluorescence of a glucose-specific protein (fluorophore). The fluorophore is capable of re-emitting light at longer wavelength when excited with light. Concanavalin A (ConA), dextran, α-methyl mannoside and glycated protein are examples of fluorophores which can be used to bind with glucose molecules and act as an indicator [21]. The technology is extremely sensitive and can sense even a single molecule.

1.4.2.b) Miscellaneous Methods

i) Reverse Iontophoresis

Iontophoresis is based on the principle of electro-osmosis in which an electric potential is applied for ion transportation across the skin. The low current flow (<0.5 mA/cm^2) between the anode and cathode of the voltage source is

facilitated by the flow of ions (sodium and potassium) towards the surface of the skin [27]. The flow of ions is also accompanied by uncharged molecules like glucose from the interstitial fluid which is collected at the cathode. The cathode also doubles as a traditional glucose sensor which can then sense the physiological glucose level.

The major limitation is skin irritation and rash caused by interstitial fluid transportation. Also, the concentration of glucose thus collected is very low and does not reflect rapid changes in blood glucose levels. The sensor has to be regularly replaced from time to time to ensure hygienic condition.

ii) Other body fluids

A lot of research work has gone into checking the feasibility of sensing glucose levels in body fluids such as a tear, saliva and urine. Research groups have come up with contact lenses (disposable/reusable) capable of either measuring/indicating the glucose level in tear [28], [29]. Colour changing dipsticks have also been used to measure the glucose levels in urine.

These methods lack real-time monitoring of blood glucose levels. Often in diabetic patients with healthy kidneys, hyperglycemia is not reflected in urine. The correlation between blood glucose level and the glucose content in tear and saliva is still a subject of study and has not been perfected [30].

1.4.3 Minimally-invasive blood glucose monitoring

There is no clear boundary in differentiating minimally invasive techniques from invasive ones. Minimally invasive techniques can be called as a group of techniques which either access interstitial fluids (tissue fluid) or blood from

capillary vessels thus avoiding hypodermic needle and the damage associated. The sample volume required by these methods would be of the order of several microlitres (μL) only.

1.4.3.a) Glucometers

A blood glucose monitor (BGM) or glucometer as shown in figure 1-7 is an electronic device for measuring the level of glucose in the blood. A relatively small drop of the order of tens of microlitre blood is placed on the chemical layer of a disposable test strip. The strip is then interfaced with a digital meter. Within several seconds, the level of blood glucose will be shown on the digital display.

In the first generation of electrochemical sensor, the biosensors rely on the measurement of oxygen consumed or on detection of hydrogen peroxide generated. The electrochemical reaction is similar to as shown in equation 1 and 2.

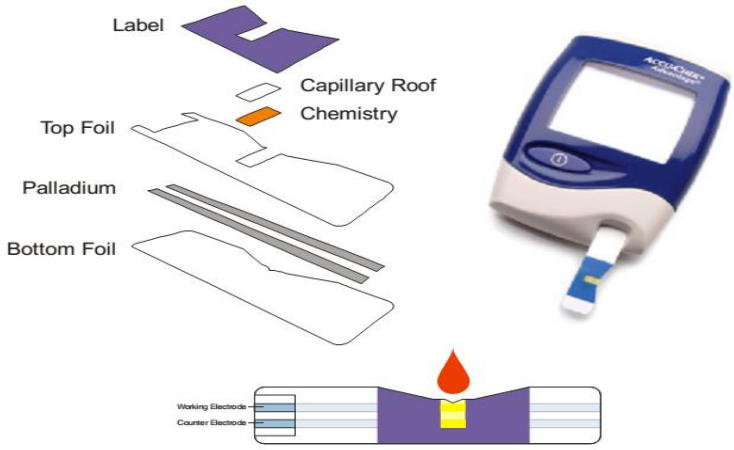

Figure 1-7: Structural details of BGM strip.

Figure source: Roche Products Limited and Roche Diagnostics Limited

For anodic (amperometric) measurement of hydrogen peroxide, a relatively high common working electrode potential has to be applied. With such high potential, other blood constituents such as ascorbic acid, and uric acids and some drugs (e.g., acetaminophen) can become electroactive which can lead to an erroneous result. Secondly, the dependence of oxygen as a physiological electron acceptor is subjected to error arising from the fluctuation and stoichiometric limitation of oxygen [31], [32].

In the second generation, as shown in figure 1-8, mediators are used in the process of enzyme oxidation. Mediators are special organic or inorganic compounds with low molecular weight capable existing in both reduced and oxidised form.

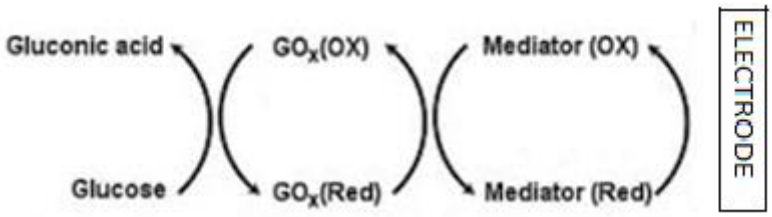

Figure 1-8: Working principle of a second generation electrochemical sensor[18]

The third generation biosensors are based on direct electron transfer between glucose reagent and electrode. These sensors have very low operating potential (+0.2 to +0.4 V) and have all the advantages of the second generation sensors. These sensors can also be classified as solid-state sensors.

$$GOD\ (FADH_2) \xrightarrow{\text{Organic Salt}} GOD(FAD) + 2H^+ + 2e^- \qquad (7)$$

GOD = Glucose oxidase

$FADH_2$ = Reduced flavin adenine dinucleotide

FAD = flavin adenine dinucleotide

Here special conducting organic salts act as the electrode. The reaction shown in equation (7) does not depend on oxygen concentration. These sensors are relatively new and have not been tested *in vivo* due to their biocompatibility issues [32].

Enzyme	***Coenzyme***	***Additional Enzyme***	***Mediator System***	***Indicator***	***Product examples***
GOD	FAD	POD	Air oxygen/hydrogen peroxide	Leuco dye	Chemstrip bG, One Touch
GOD	FAD	None	Hexacyanoferrate III /Hexacyanoferrate II	Palladium electrode	Accu-Check Advantage
GOD	FAD	None	Hexacyanoferrate III /Hexacyanoferrate II	Carbon electrode	One Touch Ultra
GDH(GlucDOR)	PQQ	None	Hexacyanoferrate III /Hexacyanoferrate II	Palladium electrode	Accu-Chek Advantage (Comfort Curve strip)
GDH(GlucDOR)	PQQ	None	Quinoneimine/ phenylendiamine	Phosphomolybdic acid	Accu-Chek Active, Accu Chek Compact, Accu-Chek Go
GDH(GlucDOR)	PQQ	None	Quinoneimine/ phenylendiamine	Gold electrode	Accu-Chek Aviva
GDH(GlucDOR)	PQQ	None	Osmium	Electrode	FreeStyle
GDH	NAD	None	Phenanthroline quinone	Electrode	Precision Xtra
GDH	FAD	None	Hexacyanoferrate III /Hexacyanoferrate II	Palladium electrode	Ascensia Microfill

Figure 1-9: Some of the enzyme and mediator systems being used in different products [31]

Even though glucometers are commercially successful and many manufacturers have their own version of the device, they are not completely fail-safe. As several researchers [21], [33] have shown that in patients with rare diseases, the presence of certain medication or other forms of sugar (maltose, xylose, galactose) can show false positive glucose readings. Also with a few intermittent measurements with BGMs, it is not possible to predict the future trends in glucose levels variation. Even with the cost of BGM being low (~£20), the cost for expendables (strip, lancet, etc.) can accumulate over a period of time.

1.4.3.b) Continuous Glucose Monitoring system (CGMs)

Type 1 diabetic patients and extreme cases of Type 2 diabetic patients are required to check their blood glucose levels regularly for delivering the correct dosage of medication. CGMs use indwelling sensors to access interstitial fluids for measuring glucose levels. These sensors are implanted subcutaneously into the abdominal wall or arm.

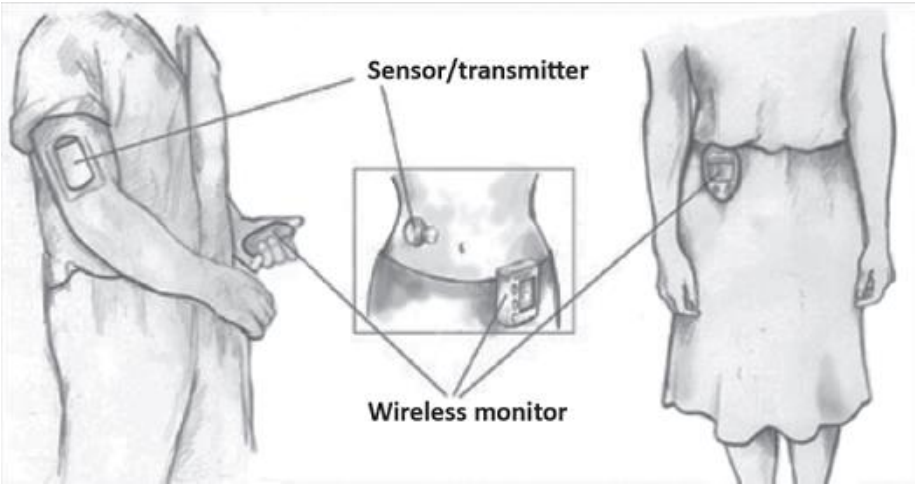

Figure 1-10: CGM system

Source: https://thediabeticnews.com/type-1-diabetic-adults-should-use-cgm-experts-say/

A small light weighted radio transmitter is attached to the sensor for acquiring the glucose level values and for transmitting it to a wireless monitor which can then store the values for post-processing. CGMs are capable of monitoring glucose levels, its trend, and also raise alarm in an event of any abnormalities.

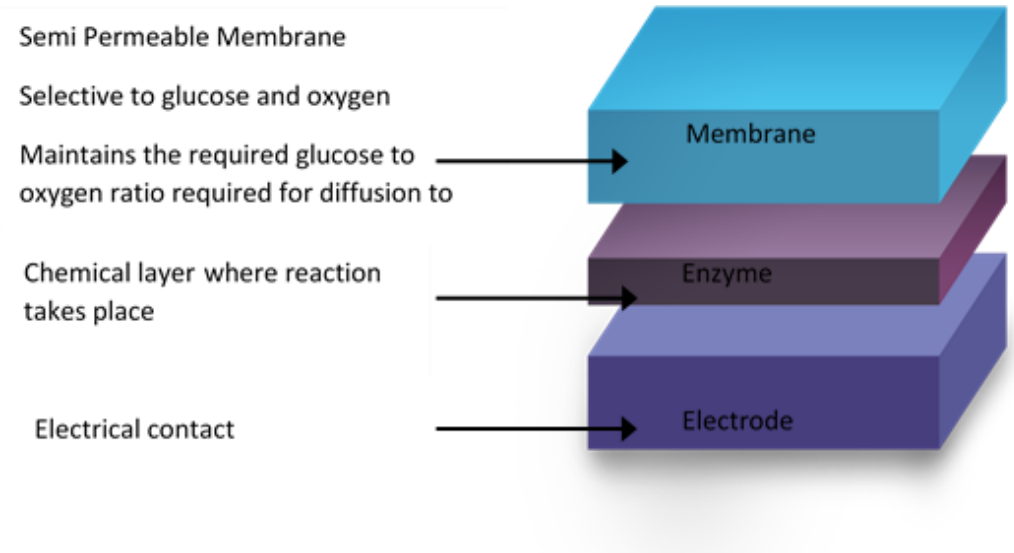

Figure 1-11: CGM sensor components

Figure 1-11 shows the CGM sensor components. It consists of a semipermeable membrane, the enzymatic layer and electrode. The semipermeable membrane is capable of selectively diffusing glucose to the enzyme layer for electrochemical reaction. It is also responsible for the biocompatibility. Amperometric measurement is done at the electrode for measuring glucose levels [32], [34].

Even though CGMs are helpful for continuous glucose measurements there are also drawbacks;

- Not real time monitoring- Interstitial glucose levels lag blood glucose levels [35].
- Biocompatibility - Undesirable interactions between the surface of the implanted device and biological medium cause deterioration of the sensor performance and hence requiring frequent replacements (3-7 days) [36].
- Cost- Most insurance companies currently view this as an experimental treatment [3].
- The sensor has to be calibrated frequently and requires BGMs [37].
- Not accurate enough to place CGM and Insulin pump in a closed circuit.

1.4.4 Boronic acid-based glucose measurement methods

Boronic acids are known to bind with compounds containing diol moieties through reversible ester formation with high affinity. Such tight binding will allow boronic acid to be used in the construction of sensors for saccharides [38]-[43]. However, the stability of the boronate ester is pH and solvent

dependent, and factors governing these processes are not well understood [38], [41].

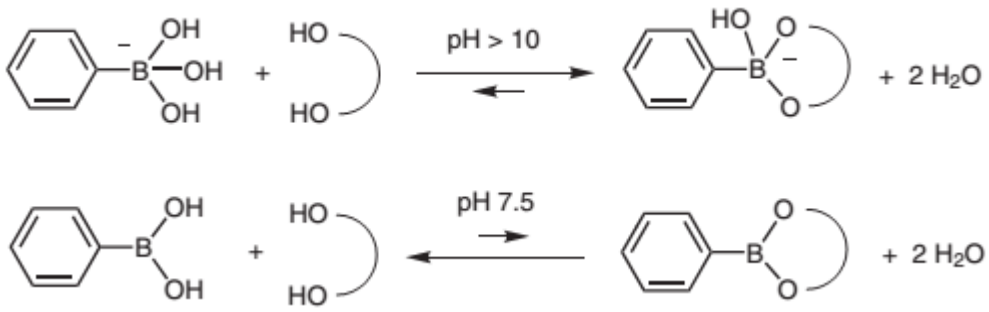

Figure 1-12: Equilibrium formation of boronic esters from diols at high and neutral pH in water [42]

Equilibrium of boronic acid in water is shown above. For stable binding, tetrahedral/dissociated form is preferred due to the stabilization of the structure by bond relaxation from 120^0 to 109^0 [42]. Different substituents have a significant effect on boronic acid. An electron withdrawing group (EWG) decreases the pKa while electron donating groups (EDG) will increase the same. Hence different substitution can be used to tailor the properties of boronic acid [41]. This also gives boronic acid the capability to form reversible complexes which are pH dependent. Further to this, in a research by Huseyin Sakalak et.al, [44] cytotoxicity studies of boronic acid-carrying poly(methyl methacrylate) nanoparticles were carried out in 3T3 cells which showed no toxicity effect on the cells.

1.5 Project overview

1.5.1 Research gap

From the literature review, it is evident that there is further scope for improvement and need for new sensing approach especially based on optical

methods. So far optical approaches have been sought mainly for non-invasive techniques. Only very little research has gone into developing minimally-invasive blood glucose monitoring based on optical approaches. Sensing platform based on fibre optics and fluorescence methods are long known for its capabilities for sensing refractive index [45], [46], pH [47], chemical compound, gas, ions [48] and also for imaging [49]. It is also resistant to the corrosive environment and since the signal carried is optical, it is not affected by electromagnetic interference [50]. Reinforced optical fibre can be used both for piercing and as a probe for different spectroscopic techniques. Suitable materials can be used to design fibre to make it biocompatible. The use of optical fibre will, in turn, minimize the scattering and absorption of the optical signal by tissue and give a higher signal to noise ratio. Microstructured fibre (MSF) is another speciality fibre whose unique features and design flexibilities can be utilized for this purpose. Development in boronic acid-based sensors has been a central theme for various researchers working in the field of glucose sensing. Interestingly the capability of boronic acid to form a strong reversible covalent bond with diols, tunability of sensitivity and selectivity can be used in this research. Further to this, the low toxicity of boronic acid is an added advantage for this research.

1.5.2 Research aim & objectives

This research aims at recommending a novel minimally-invasive blood glucose sensor based on microstructured optical fibre. The project intends to integrate the principles of optical fibre technology (single, multicore and multi-structured) to increase the sensitivity, reliability and spectroscopic methods (IR spectroscopy and fluorescence technology) for higher sensitivity. The

research aims to use poly(methylmethacrylate) or PMMA as the polymer matrix to immobilize boronic acid moiety.

Research objectives are given below.

1. Mathematical modelling and simulations to design and optimize fibre structure for maximizing evanescent power fraction and field interaction volume.
2. The investigation into boronic acid-based glucose sensing.
3. Compatibility of the chosen reagent with an optical sensing method.
4. Fibre optic sensor development.
    a) Realization of the fibre structure
    b) Immobilization of reagent to fibre.

Chapter 2 - Theory

2.1 Mathematical analysis

2.1.1 Theory and design parameters of the optical fibre

2.1.1.a) Principle of operation

The optical fibre (fibre optics) is a cylindrical waveguide made of dielectric material. It is flexible, transparent and is capable to transmit visible and infrared wavelengths of the electromagnetic spectrum. It consists of a transparent core surrounded by a cladding material of lower refractive index. Optical signal coupled to the fibre core under certain condition allow them to propagate by the principle of total internal reflection.

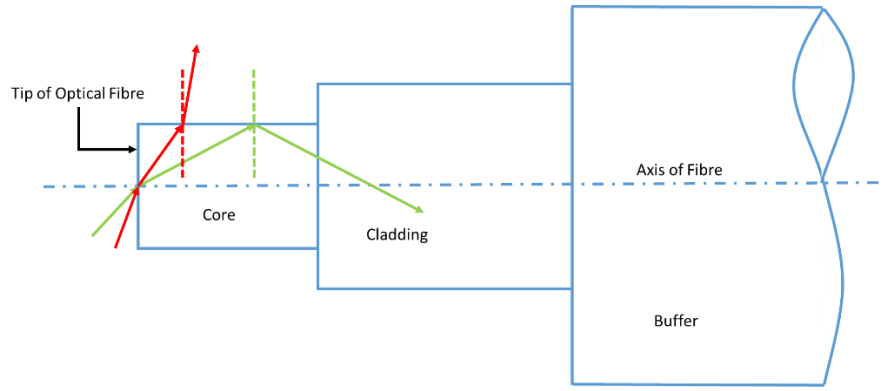

Figure 2-1: Launching of light into the optical fibre

(adapted from NPTEL[51])

The green ray in figure 2-1 represents light propagating through the optical fibre and the red ray represents light escaping from the core of the optical fibre.

2.1.1.b) Total internal reflection (TIR)

TIR is a phenomenon by which light travelling in a medium reflects off the boundary. In order for TIR to happen, the ray must be travelling from a denser medium to rarer medium and the angle of incidence should be greater than the critical angle. Total internal reflection can be explained by the ray model which obeys Snell's law. Figure 2-2 below depicts typical refraction and reflection phenomena taking place at the interface between two different materials having refractive indices n_1 and n_2.

2.1.1.c) Critical angle

Critical angle is defined as the incident angle at which the refraction occurs at an angle of 90^0. This is the largest angle above which TIR happens.

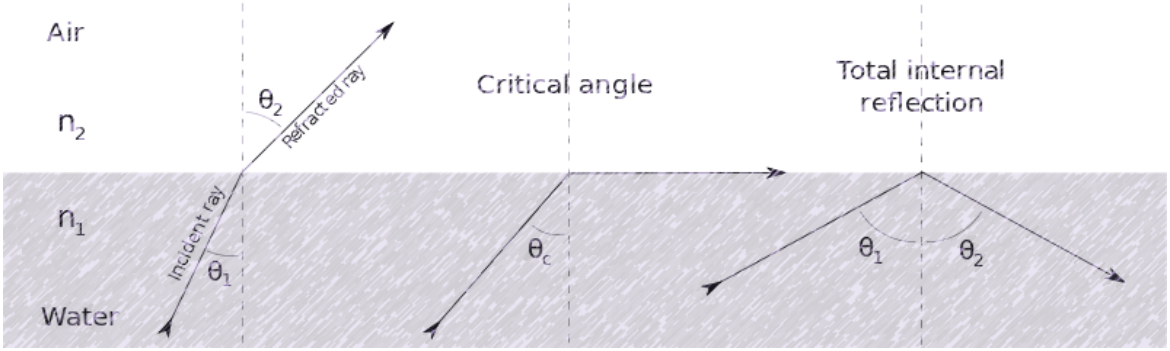

Figure 2-2: Effect of incident angle on refraction of light at the interface between two media. The figure also shows the effect of TIR

Source: https://en.wikipedia.org/wiki/Total_internal_reflection

In the situation of TIR, ie, when the incident angle θ_i (θ_1)> critical angle θ_c,

$$\theta_c = sin^{-1}(\frac{n_2}{n_1}) \quad (8)$$

the transmitted (refracted) ray will not exist. Even though the total energy of the beam is reflected when $\theta_i > \theta_c$ there still exist a disturbance in the second medium whose electric field decays exponentially with distance from the dielectric boundary and whose propagation direction is along the dielectric boundary. This penetration of electric field beyond the boundary is called the evanescent field.

The properties of evanescent wave can be derived from the phase factor of the transmitted wave in the second medium

Electric field E associated with the transmitted wave is given as [52]

$$\mathrm{E} = E_0 e^{-i(k_t . r - \omega t)} = E_0 \text{Þ} \tag{9}$$

where $\boldsymbol{k_t}$ is the wave vector associated with the transmitted wave. From Figure 2-3, r is given as

$$r = z sin\theta_t + y cos\theta_t \tag{10}$$

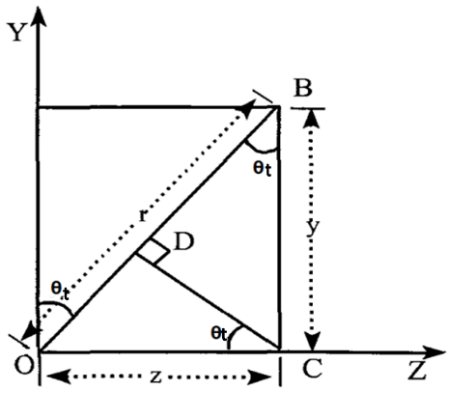

Figure 2-3: Relation between rectangular co-ordinates (Y,Z) and distance r measured from origin O.[52]

Phase factor 'Þ' from equation (9) is given as

$$Þ = e^{-i(k_t.r-\omega t)} \tag{11}$$

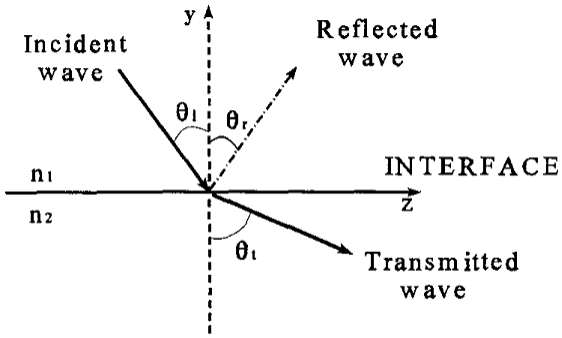

Figure 2-4: Light ray incident on the dielectric interface showing transmission and partial reflection. [52]

θ_i, θ_r, θ_t are the angles of incidence, reflectance and transmission respectively. Here $n_1 > n_2$

$$Þ = e^{-i(k_t.(zsin\theta_t+ycos\theta_t)-\omega t)} \tag{12}$$

we have

$$cos\theta_t = (1 - sin^2\theta_t)^{\frac{1}{2}} \tag{13}$$

$$sin\theta_t = (\frac{n_1}{n_2})sin\theta_i \tag{14}$$

therefore

$$cos\theta_t = (1 - (\frac{n_1}{n_2})^2 sin^2\theta_i)^{\frac{1}{2}} \tag{15}$$

substituting the value of $sin\theta_t$ and $cos\theta_t$ in equation (12)

$$Þ = e^{-i(k_o . n_2(z((\frac{n_1}{n_2})sin\theta_i)+y(1-(\frac{n_1}{n_2})^2 sin^2\theta_i)^{\frac{1}{2}}))} . e^{i\omega t} \quad (16)$$

Now consider the condition for TIR i.e $\theta_i > \theta_c$. Then $cos\theta_t$ term becomes imaginary

$$Þ = e^{-k_o . n_2 y[(\frac{n_1}{n_2})^2 sin^2\theta_i - 1]^{\frac{1}{2}}} . e^{-ik_o . n_2 z \frac{n_1}{n_2} sin\theta_i} . e^{i\omega t} \quad (17)$$

The above equation can be made compact by substituting

$$\gamma = k_o . n_2[(\frac{n_1}{n_2})^2 sin^2\theta_i - 1]^{\frac{1}{2}} \quad (18)$$

where γ is the attenuation coefficient [51], [53]

$$\beta = k_o . n_1 sin\theta_i \quad (19)$$

where β is the propagation coefficient [51], [53]. Equation (17) becomes

$$Þ = e^{-\gamma y} . e^{i\beta z} . e^{i\omega t} \quad (20)$$

Substituting the phase factor back into the equation (9)

$$E = E_0 . e^{-\gamma y} . e^{i\beta z} . e^{i\omega t} \quad (21)$$

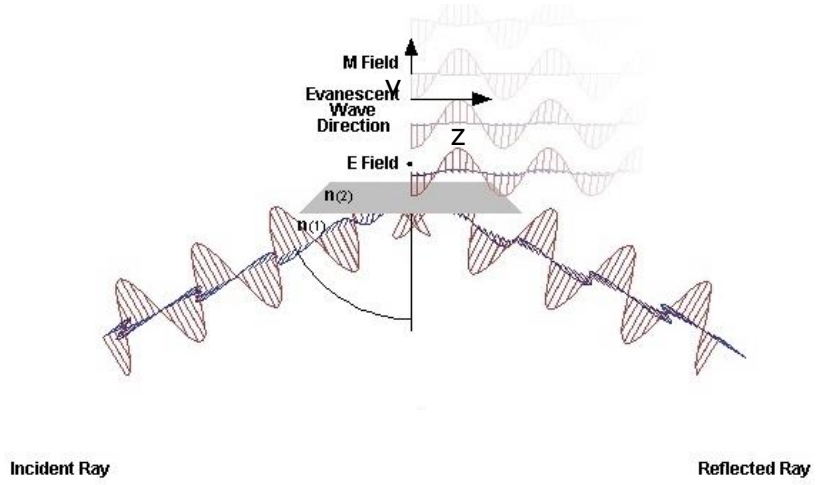

Figure 2-5: Shows the evanescent field generation and propagation

(adapted from microscopy research centre [54])

Here, γ gives an estimate of the exponentially vanishing electric field in y direction while β, propagation constant showing the evanescent wave propagation along the z direction.

2.1.1.d) Evanescent wave sensing

Optical evanescent based sensing is primarily based on two methods, the first direct spectroscopic evanescent sensor. In this, the analyte can directly interact with the evanescent field in the lower refractive index region. In order for the sensor to work, the wavelength being guided must coincide with the absorption band of the analyte. Second is a reagent mediated evanescent sensor. Here an intermediate reagent will be used which will respond optically with the analyte and may be attached to the optical waveguide.

The knowledge of evanescent electric field parameters plays a crucial role in determining the sensitivity, dynamic range etc. of the fibre optic sensor to be realized. The degree of penetration of evanescent field into to the surrounding lower index sensing medium is important. This is given by the parameter d_p which is the inverse of the attenuation co-efficient discussed in equation (18) and is given by [55], [56]

$$d_p = \frac{\lambda}{2\pi n_1 \sqrt{[sin^2\theta_i - (\frac{n_2}{n_1})^2]}} \tag{22}$$

λ is the wavelength, θ_i is the angle of incidence and n_1, n_2 are the refractive indices of the denser and rarer medium respectively.

Another important parameter is the fraction of optical mode power in cladding which is available for the evanescent field. This is a very important parameter for fibre refractometer and evanescent field absorption sensor

The power density at the core-cladding interface (core radius =ρ) is given by [57]

$$P(\rho) = (\frac{P}{\pi\rho^2})(\frac{v}{N}) \tag{23}$$

and the power flow in the cladding is given as [58]

$$P_{clad} = \frac{Pv}{N(2N - 2v)^{1/2}} \tag{24}$$

treating mode index 'v' as continuous and averaging the above equations we get power fraction at the interface as [57]

$$[\frac{P(\rho)}{P}]_{avg} = \frac{1}{\pi\rho^2 N}\int_0^N \frac{v}{N}\, dv = \frac{1}{2\pi\rho^2} \tag{25}$$

from the equation above its clear that the quantity is independent of parameters N, v and only depends on the fibre core radius [57], [59], [60].

$$r = [\frac{P_{clad}}{P}]_{avg} = \frac{1}{N}\int_0^N \frac{vdv}{N(2N-2v)^{1/2}} = \frac{4}{3}N^{-\frac{1}{2}} = \frac{4\sqrt{2}}{3V} \tag{26}$$

where V is the normalized frequency given by [50], [61]

$$V = k_0\rho\sqrt{{n_1}^2 - {n_2}^2} \tag{27}$$

ρ is fibre core radius and k_0 is the wave vector in free space

By analysing the above equations it is clear that, a high power fraction is achieved in fibres with low V parameter i.e. single mode fibre (SMF). Even though the SMFs have higher power fraction due to the ease of handling and higher power through put multi-mode fibres (MMF) are preferred. From equation (26) it is clear that, the value is higher in higher order modes (closer to cut-off) which can be achieved by launching light at an incident angle closer to the critical angle.

In an optical fibre, the evanescent field power can be tapped by removing the cladding of length L from the fibre. The portion of uncladded fibre becomes the site for evanescent wave sensing.

Optical power transmitted by an uncladded fibre in an absorbing medium is given by [59], [60]

$$P(L) = P(0)\exp(-\gamma L) \tag{28}$$

$P(0)$ is the power transmitted in the absence of an absorbing medium (initial optical power launched) and γ is the evanescent field absorption coefficient.

'γ' is related to bulk absorption coefficient 'α' by [62]

$$\gamma = r\alpha \tag{29}$$

r is the power fraction outside the core when all bounded modes are excited in an optical fibre.

substituting the value of γ in equation (28)

$$P(L) = P(0)\exp(-r\alpha L) \tag{30}$$

Evanescent wave absorbance is given as

$$A = log_{10}\frac{P(0)}{P(L)} \tag{31}$$

$$A = \frac{\gamma L}{2.303} = \frac{r\alpha L}{2.303} \tag{32}$$

where L is the length of the uncladded fibre.

2.1.1.e) Summary

Equations above suggest that the sensitivity of evanescent based fibre optic sensor depends on various parameters like incident angle (mode-order), fibre core diameter, refractive indices of core, cladding and the wavelength of light. However, for a given fibre geometry maximizing the evanescent power fraction 'r' and interaction 'L' is of utmost importance. Different research groups have tried increasing the sensitivity introducing changes in geometry by bending, tapering [63] and microstructuring [64]-[67].

2.1.2 Modelling of evanescent power fraction (r_v) in multimode optical fibre (MMF)

As discussed earlier fraction of power associated with a mode is given by equation (24)

$$r_v = \frac{v}{N(2N - 2v)^{1/2}} \tag{33}$$

A fibre of radius of 10 μm has been assumed to be in aqueous solution. Refractive index of fibre core has been considered as 1.46 with that of water as 1.33 V-Parameter has been calculated as 37.821 at a wavelength of 1000 nm. Number of modes supported by the fibre is given by [52]

$$\boldsymbol{N \approx \frac{V^2}{2}} = 715 \tag{34}$$

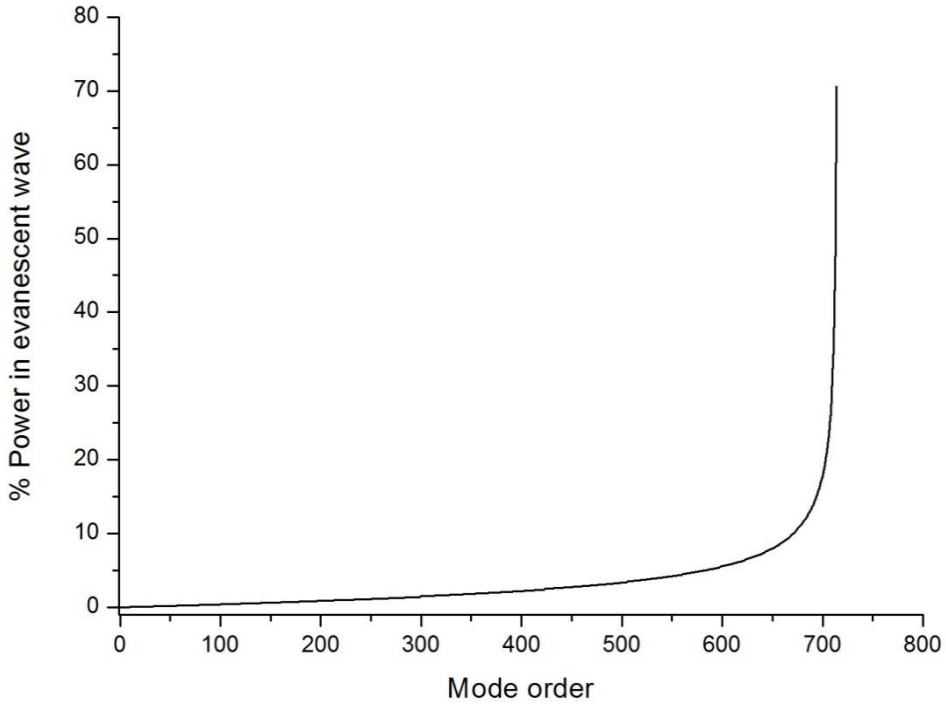

Figure 2-6: Fraction of evanescent power (r_ν) vs mode order

Mathcad calculation confirms that higher order mode contributes more to the evanescent field power than the lower ones. The study clearly suggests that it is critical while launching power to either fill the numerical aperture or to selectively excite higher order modes.

2.1.3 Analysis of evanescent field enhancement in microstructured optical fibre (MSF)

Evanescent wave sensing utilizes the exponentially decaying electric field of evanescent waves generated at the interface between dielectric media of an optical fibre. In order for the analyte to access the decaying electric field in normal optical fibre, the cladding has to be removed. The sensitivity of such a sensor is limited due to the fact that field – sample interaction is exterior to

the optical fibre. The limited length of cladding removed and large fibre diameter [68] are other factors affecting sensitivity.

The sensitivity of such a sensor can be improved by using microstructured optical fibre (MSF) or also known as holey fibre [69], [70]. A holey fibre has a cladding comprising of air-holes which can provide additional interaction volume for the same length of the fibre. This will allow analyte (liquid or gaseous) to interact more with the electric field [70].

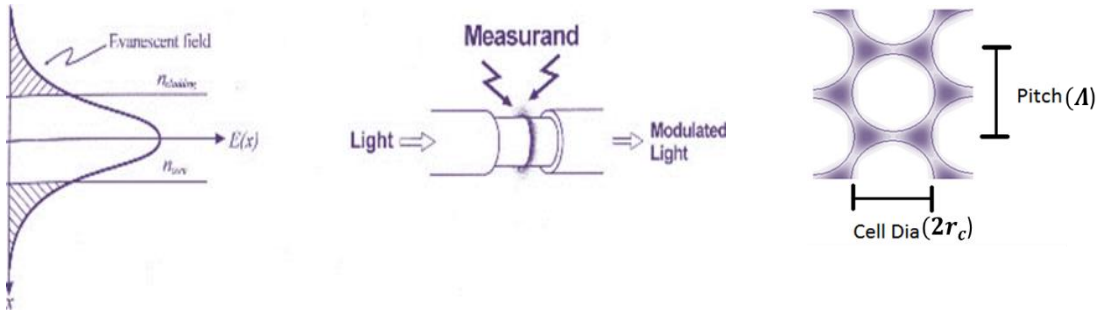

(a) (b)

Figure 2-7: (a) Evanescent field in MMF [99] (b) Electric field in MSF core

Interaction volume is defined as the sample volume which can be effectively probed with the evanescent electric field. Interaction volume for MMF can be defined as the cylindrical volume exterior to the fibre with thickness 'd_p' and sensor length 'L'.

Interaction volume for multimode optical fibre (MMF) is given by

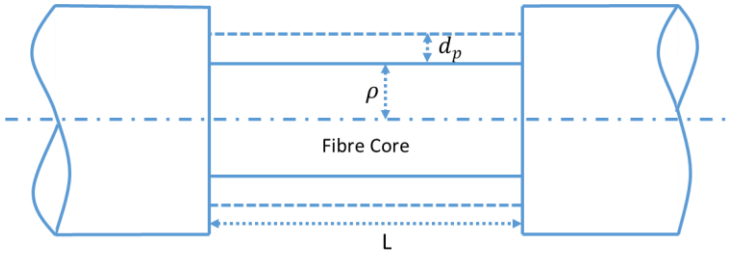

Figure 2-8: Shows the depth of evanescent wave penetration from uncladed MMF of length 'L'

$$\{\pi(d_p + \rho)^2 - \pi\rho^2\}L$$

$$Interaction\ Volume\ (V_{MMF}) = \pi L d_p(2\rho + d_p) \quad (35)$$

ρ, d_p are MMF core radius and evanescent field penetration depth respectively. It can be seen from the equation (35) above that for given MMF fibre sensor geometry there is not much design flexibility for increasing V_{MMF} other that changing the wavelength 'λ', and mode being excited.

The air holes in MSF Figure 2-7 (b) act as sites for the analyte to interact with the strong evanescent field. As a result, for the same length of fibre sensor, an electric field enhancement of several orders is achieved in MSF due to the increased surface area and interaction volume through its hollow core and the cells in the cladding.

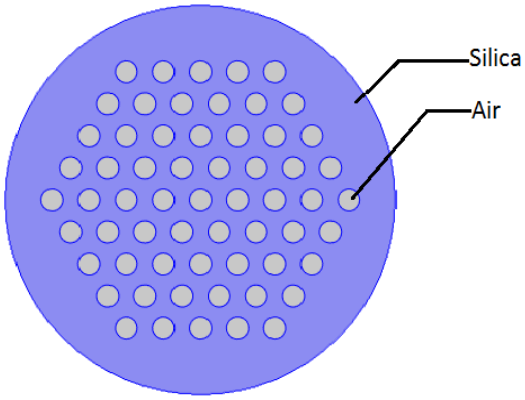

Figure 2-9: Cross-sectional view of MSF with N_{core} = 1

In holey fibres, the analyte can interact in three different regions. First in the hollow core region, second in the hollow cells in the cladding and third outside the holey fibre similar to the MMF. The size of the hollow core is designed by collapsing multiple cells in core given by N_{core}. Commercial holey fibres have typical N_{core} values of 7, 19 cells [71] but are not limited. The air cells are assumed to be arranged in a hexagonal packing which has a maximum packing efficiency (P_f) of 90.69% [72].

Number of air cells in the holey fibre cladding (N_{clad}) for given core radius 'ρ' and pitch 'Λ' is given by

$$N_{clad} = 4P_f\left(\frac{\rho^2}{\Lambda^2}\right) - N_{core} \tag{36}$$

Interaction volume (V_{clad}) for number of holes (N_{clad}) in the cladding region is given by

$$V_{clad} = N_{clad}(\pi {d_p}^2(1 - \frac{2r_c}{d_p})) \tag{37}$$

Where 'r_c' is the cell radius

Interaction volume obtained for hollow core (V_{core}) is given by

$$V_{core} = \pi L {d_p}^2 (1 - \frac{\Lambda}{d_p}\sqrt{\frac{N_{core}}{P_f}}) \quad (38)$$

the distance between the cell as shown in figure 2-7(b)

Total interaction volume (V_{MSF}) is given as

$$V_{MSF} = V_{MMF} + V_{core} + V_{clad} \quad (39)$$

For the purpose of comparing the excitation parameters incident angle, the wavelength is taken same ($\theta_i = 50^0, \lambda = 800\, nm$) also both fibres have same the radius ($\boldsymbol{\rho = 100\, \mu m}$) and interaction length ($\boldsymbol{L = 2\, cm}$). Fibre material is considered to be fused silica.

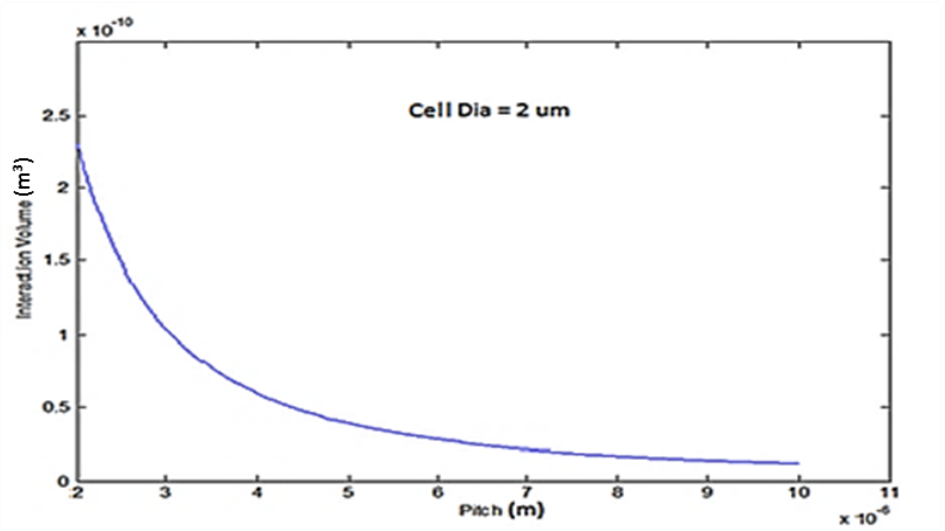

Figure 2-10: Variation of interaction volume with pitch in microns

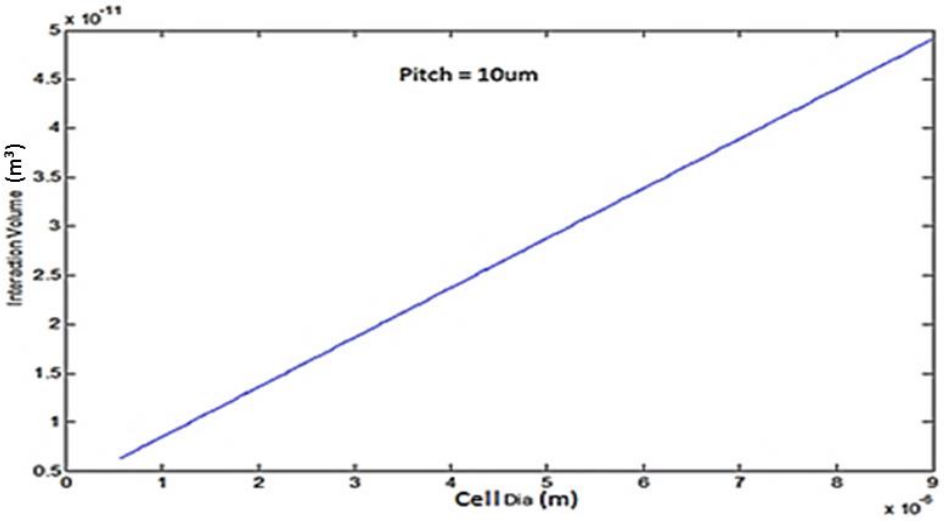

Figure 2-11: Variation of interaction volume with cell diameter

Figure 2-10 and Figure 2-11 above show the influence of pitch and cell diameter on interaction volume. A decrease in interaction volume is observed with increase in pitch between the cells. This is mainly due to the fact that number of air cell 'N' is inversely proportional to the pitch. On the other hand, a linear increase in interaction volume is observed upon an increase in cell diameter.

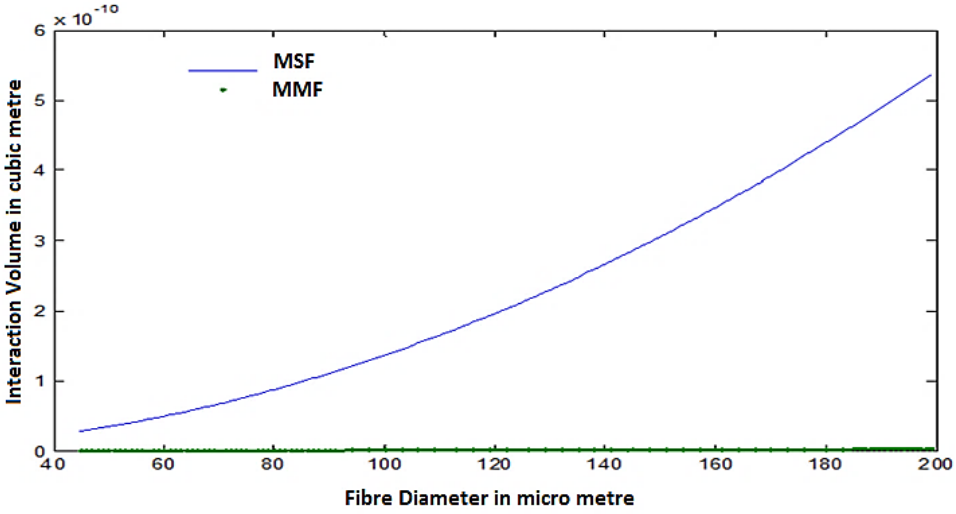

Figure 2-12: Compares the variation in field-analyte interaction volume between MSF and MMF.

Figure 2-13 compares the variation in the field–analyte interaction volume between MSF and MMF upon increasing fibre diameter. A significant enhancement in field-analyte interaction volume was achieved using MSF.

MSF has shown an enhancement factor of several orders in interaction volume when compared to MMF and is a function of its pitch and cell diameter. This results in an increased evanescent electric field interaction with fluorophore and analyte leading to a higher sensitivity. The analysis also confirms the enhancement of evanescent wave electric field through the use of microstructured optical fibre. Additional enhancement in evanescent power fraction along boundary connecting the cells (microstructure) is expected by considering equation (32). This is because the cell wall thickness is of the order of few fractions of micrometre mimicking the properties of SMF without compromising structural integrity.

2.2 COMSOL simulations

Modelling and simulation of fibre structures often involve inherent structural and mathematical complexities in solving Maxwell equation, due to which analytical solutions are not possible [73]. Fully vectorial finite element software COMSOL Multiphysics version 4.4 has been used for carrying out numerical simulation here. Finite element method (FEM) is a powerful mathematical tool and has been successfully used to solve field pattern in optical fibre numerically [74]. Modelling of optical fibre depends on the assumption of translational invariance along the propagation direction [75]. This symmetry with proper assumptions helps to contain the modelling of the optical fibre to a 2D simulation of the cross-section thereby reducing the computational complexity.

2.2.1 Simulation of PMMA coated MMF fibre for evanescent sensing in aqueous media and the effects of bending on its performance.

In reagent mediated evanescent sensor an intermediate reagent will be used which responds optically with the analyte and may be attached to the optical waveguide. One of the methods, other than the use of silane coupling agent [76]-[78] is to coat the uncladded fibre surface with the polymer (PMMA) to which the reagent can be immobilized. The other method is to create a reagent doped polymer layer over the sensor surface. An increase in sensitivity is expected with reference to equation (25),

$$r = \frac{1}{2\pi\rho^2}$$

PMMA layer of 20 µm (thickness of dip coating) has been considered in this simulation. Here numerical simulation has been carried out to understand the effect of polymer coating on the uncladded hard clad fibre (HCF) of core diameter 200 µm and the numerical aperture of 0.37. Computational work has been carried out using three different fibre geometries, hard clad fibre (HCF, core refractive index= 1.46483 & cladding refractive index = 1.4173), cladding stripped HCF (bare fibre or BF) and proposed PMMA coated fibre (Inverted Trench Fibre or ITF). The effect of bending on sensor performance is also been analysed.

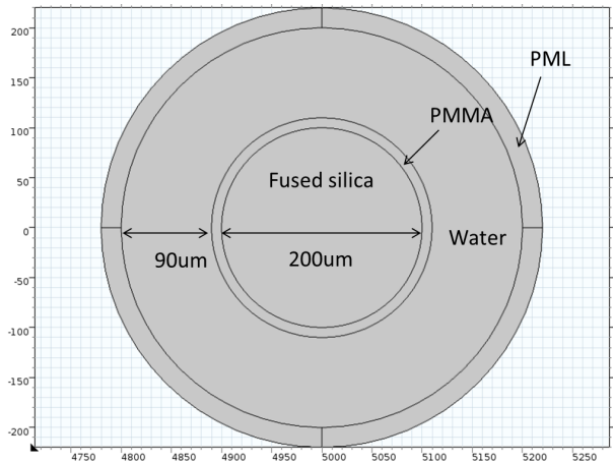

Figure 2-14: Simulated geometry of proposed PMMA coated evanescent sensor in aqueous solution.

$n_{fused\ silica}$ = 1.46483, n_{pmma} = 1.49913 and n_{water} =1.33 [79]-[81]

The aqueous region has been modelled with a thickness of 90 µm. Perfectly matched layer (PML) of thickness 20 µm has been created in the extremities to simulate open boundaries and avoid any unwanted reflection [82], [83].

The effect of curvature introduced by bending on the sensor can be taken care of by proper coordinate transformation (conformal mapping) as described by

Heiblum & Harris [84]. Modelling of the sensor structure in an aqueous environment was implemented in 2D-axisymmetry in order to compensate for the additional path length introduced by bending. The transverse plane of fibre cross-section is in the r-z plane and the fibre bent is in a ψ-r plane making ψ as the propagation direction of the wave. Evanescent power fraction η in ψ direction is expressed as [85]

$$\eta = \int_{water}^{same\ mode} (E_x H_y - H_x E_y) dxdy \Big/ \int_{Total}^{same\ mode} (E_x H_y - H_x E_y) dxdy \qquad (40)$$

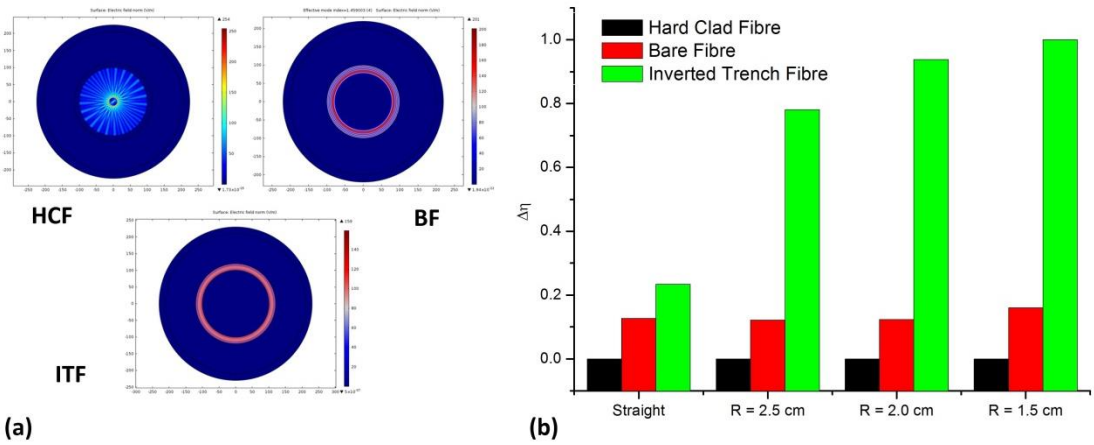

Figure 2-15: (a) Computational images of the electric field distribution in HCF, BF and ITF, and (b) change in power fraction, *Δη*, of HCF, BF and ITF for straight and different bend radius R

Figure 2-15 (a) shows the electric field distribution in HCF, BF and ITF in a straight configuration. In HCF E-field is confined in the centre of the fibre core, while in BF, fibre modes go under transition to whispering gallery modes (WGM) and confine towards the surface [86]. In the case of ITF, due to the PMMA layer having a higher refractive index, all the E-field confines to the thin PMMA layer. This unusual refractive index profile can be considered as an inverted trench fibre.

Effect of bending has been carried out by bending the HCF, BF and ITF at radii R = 2.5, 2.0 and 1.5 cm. A bend radius of less than 1.5 cm can physically damage the fibre and hence taken as the lower limit. Significant enhancement in $\Delta\eta$ is achieved for bend radius below 2.5 cm and hence R = 2.5 cm is taken as an upper limit. In figure 2-13(b) results indicate that Δη increases by 6 fold for the R = 2.5cm (compared to straight) and further increases with reducing the R, which is very significant for the evanescent sensors. Due to the mode transformation to WGM, radiation losses due to bending was absent [63], instead, it caused mode field to concentrate toward the outer surface of bend creating high power fraction at the dielectric boundary and hence also in water.

ITF has been long used to device high Q-factor microresonators for amplified spontaneous emission (ASE) [87]. According to literature search, ITF geometry has never been used for evanescent field sensing, making it novel.

2.2.2 Simulation of liquid filled microstructured hollow core-polymer optical fibre

Micro-structured optical fibre or holey fibre offers huge potential in the field of fibre optic sensing for biochemical or chemical species [67]. The guidance in hollow core - polymer optical fibre (HC-POF) is primarily based on photonic band gap (PBG) effect in which the air hole surrounding the fibre core acts as photonic crystals. Due to the PBG effect, liquids or gases with the lower refractive index can be used to fill the core without changing the guidance mechanism [69], [88], [89]. The hollow core together with the holes running through the cladding region can be filled with liquid samples. Parameters like polarization, wavelength, intensity and phase of the mPOF will be modified by

the direct interaction of samples with the mode field in the hollow core and/or with the evanescent field in the holes of the cladding. As a result, parameters of interacting liquid with the field can be quantified [90]. These arrays of liquid-filled holes can be designed in suitable ways so that certain wavelengths are not allowed to penetrate and hence can be confined in the core. The optical mode field confinement within the liquid core can be controlled by varying different parameters such as pitch 'Λ' and hole diameter 'd' thereby, increasing the interaction between the electric field and sample. Also, the requirement of having a high d/Λ ratio [73] makes the PBG based guidance suitable for liquid infiltration. Polymethylmethacrylate (PMMA) has been considered as the fibre material due to its unique prospects for optical fibre sensing application. The surface of polymer optical fibre (POF) can be readily modified with suitable agents which can be utilized for molecular recognition in chemical or biochemical sensing applications [91].

2.2.2.a Relative sensitivity of LC-POF (Liquid core-POF)

Relative sensitivity coefficient (r_s) for a particular wavelength is given by [85]

$$r_s = \left(\frac{n_l}{n_{eff}}\right) f \tag{41}$$

where, n_l is the refractive index of liquid species used for filling, n_{eff} is the effective index of the propagating mode and f is the fraction of power located in the liquid filled hole. The value of f is determined by the ratio of the integrated power inside liquid filled holes to the total power of the corresponding mode and is expressed as [85]

$$\mathrm{f} = \int_{holes}^{same\ mode} (E_x H_y - H_x E_y) dxdy / \int_{Total}^{same\ mode} (E_x H_y - H_x E_y) dxdy \qquad (42)$$

2.2.2.b Confinement loss ($L_c(\lambda)$)

The confinement loss $L_c(\lambda)$ for a particular wavelength is given by [85]

$$L_c(\lambda) = \frac{40\pi}{\ln(10)\lambda} Im\{n_{eff}\} \mathrm{dB/m} \qquad (43)$$

where $Im\{n_{eff}\}$ is the imaginary part of the effective refractive index and λ is the corresponding wavelength.

In order to find the relative sensitivity of LC-mPOF, the mode field pattern and the effective index of allowed core modes have to be calculated. The air holes in the LC-mPOF are arranged in hexagonal symmetry with a hole to hole distance as pitch 'Λ' and diameter of the hole as 'd'. The core radius is taken as 2.1 Λ formed by combining 19 air cells in the centre. Figure 2-16 shows the geometry of the proposed LC-mPOF. Five rings of air holes are used which is then filled with liquid.

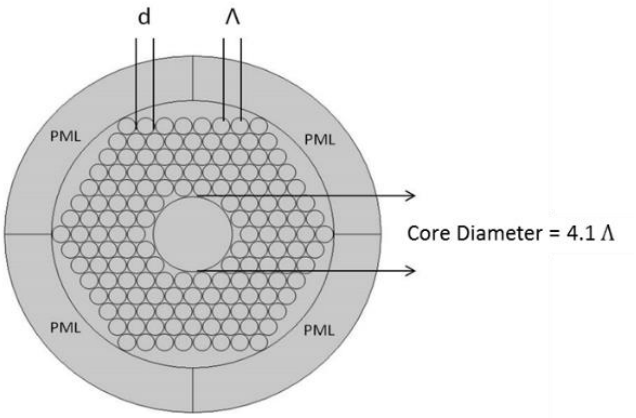

Figure 2-16: Cross section of the mPOF

2.2.2.c Simulation

Simulations have been carried out using COMSOL Multiphysics 4.4. In the simulation, the refractive index of the structure (PMMA) and liquid (water) was considered as 1.4914 and 1.33 respectively. In the study, the pitch was taken as 2 μm and d/Λ ratio was changed from 0.4 to 0.9 in steps of 0.1 by keeping a constant core diameter value of 8.2 μm. Isotropic perfectly matched layers (PML) were considered as boundary conditions.

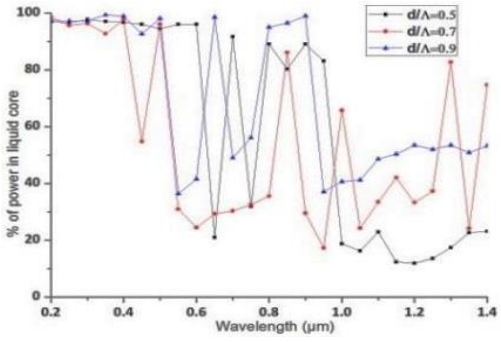

Figure 2-17: Shows the change in percentage of power fraction with respect to normalized cladding hole diameter.

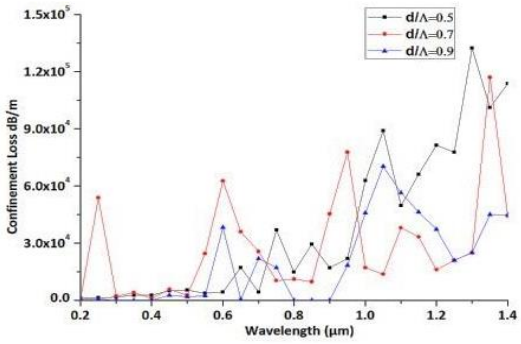

Figure 2-18: Shows the change in confinement loss with respect to normalized cladding hole diameter

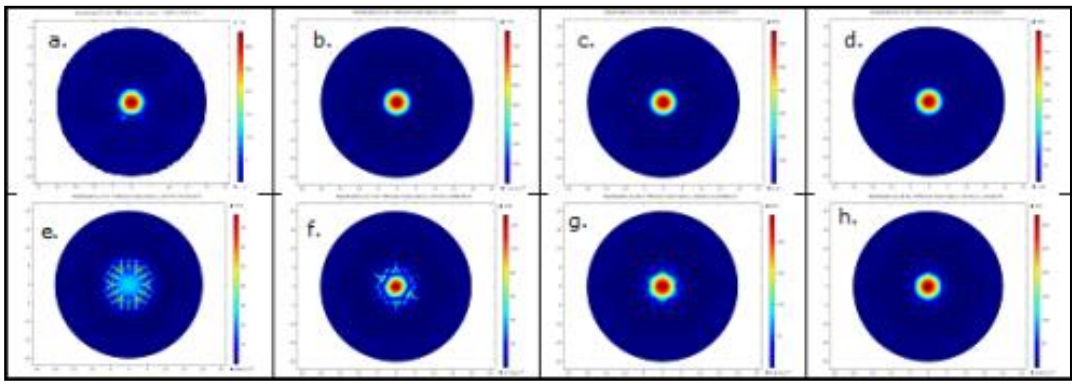

Figure 2-19: a-h Measured near field distribution

Wavelengths at 200, 300, 350, 450, 700, 750, 800, 850 nm respectively.

Figure 2-17 & Figure 2-18 show the change in the percentage of power fraction and confinement loss with respect to d/Λ ratio. To avoid the complexities in data representation only three value of d/Λ ratio have been shown in the figure. There is a general trend of reduction in confinement loss and a significant increase in the percentage of power fraction with an increase in d/Λ ratio. Hence a higher d/Λ was required for achieving lower loss and higher power fraction. In our study, we set the pitch value as 2 µm and an increase in the same will also result in higher confinement loss. An upper cut-off 0.95 was imposed on d/Λ ratio due to the onset of inherent weakness in structure which will make the fibre cells to collapse while manufacturing. Figure 2-19 (a-h) show the transverse near-field distributions of the confined mode in the liquid core at 200, 300, 350, 450, 700, 750, 800 and 850 nm wavelength respectively. Upon further studies, d/Λ ratio of 0.94 was found to be ideal in our case. Value of 'Λ' is taken as 2 µm and 'd' as 1.88 µm with a core diameter of 8.2 µm. Figure 2-20 (a) shows the confinement loss and fraction of power in the liquid core as a function of wavelength in steps of 50

nm by keeping the d/Λ ratio as 0.94. Figure 2-20 (b) shows the mode confinement for the same configuration.

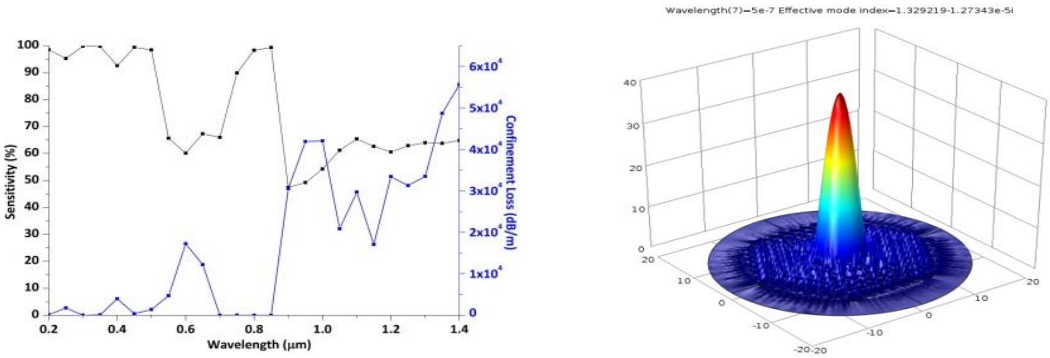

Figure 2-20: (a) Confinement loss and Relative sensitivity in liquid core at d/Λ = 0.94 (b) Mode pattern in three dimensions

It is evident that the core refractive index is lower (Water=1.33) than the effective index of cladding (1.38). In this case propagation of light is by the existence of photonic bandgap instead of modified total internal reflection (MTIR). From Figure 2-20 (a) it has been also observed that the confinement loss is minimum in UV-Visible range and higher at IR range. Due to the low confinement loss, the electric field was very much enhanced in the core region. This will in turn increase the interaction of the electric field to the liquid core in the UV-Visible region. As the effective index of the guided mode lies within the refractive index of the guiding medium (water), the trend in coefficient of sensitivity was found to be in line with the percentage of power fraction in liquid core. This special property can be utilized to make the device used for a variety of sensing applications.

From the analysis, a very high core confinement for electric field (99.84%) and a minimum confinement loss as low as 0.17 dB/km in water-filled mPOF was

achieved. The high electric field confinement in the core region for the UV-Vis range together with the potential advantages of polymer material can make the fibre a suitable candidate for glucose sensing.

2.3 Hollow optical fibre as micro-resonator for glucose sensing

2.3.1 Introduction

Evanescent wave based optical sensors interrogate the presence of analytes on the sensor surface or in the surrounding environment typically by relying on the detection of effective refractive index change. In order to increase sensitivity or to detect the very low concentration of analytes long waveguide lengths (exceeding cm) are typically required. This is required in order to accumulate a detectable phase shift and thereby increasing the signal to noise ratio [92]. These long waveguide lengths would, in turn, require a significantly large volume of samples for sensing.

Microresonators on the other hand have a unique advantage by reducing the size of the device by orders of magnitude, thereby significantly reducing the amount of sample needed for the detection. By virtue of high-quality factor (Q) resonance, the necessary interaction length can be increased without increasing the size of the device. The resonance effect provides an effective long interaction length for the sensor to achieve sufficient sensitivity.

However even with all these advantages to achieve the fluid handling capabilities, required for bio-sensing experiments the microresonator needs to be modified. To address this problem, sensors based on PMMA optofluidic ring resonator (OFRR) has been proposed as shown in figure 2-20.

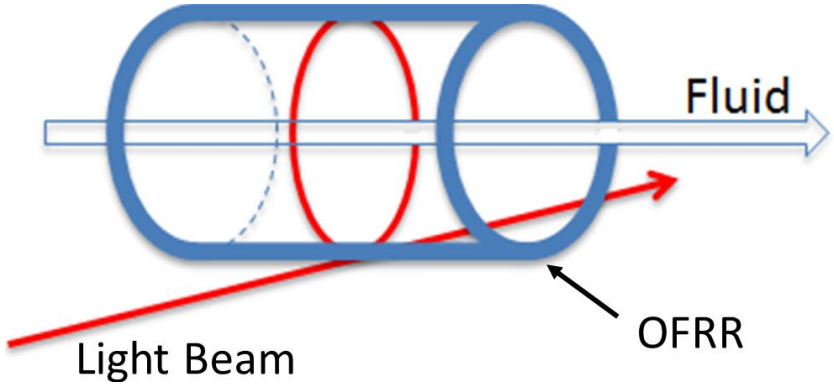

Figure 2-21: Representation of Optofluidic ring resonator

2.3.2 Theory of polymer OFRR

The confinement of the electric field to the inner surface of the microresonator is of utmost importance. The PMMA-OFRR has been fabricated by doping VPBA into MMA. The immobilization of the VPBA onto PMMA makes the surface of the OFRR to selectively bind to glucose. Glucose sensing being a surface event, it is better to restrict the probing electric field and confine to the close proximity of the surface. This further enables to OFRR to be insensitive to the inconsistency of fluid refractive index.

The time-independent field distribution for the OFRR resonance mode can be separated into two: a radial-dependent mode component and an azimuthal-dependent phase term, $\Psi_Z(r)\exp(im\varphi)$, where Ψ_Z is the amplitude of the axial magnetic (TE) or electrical (TM) modal field, m is the azimuthal quantization number.

The radial dependent field Hz can be expressed by Bessel function in the following form [93]

$$H_z = \begin{cases} AJ_m(n_1 k_0 r) & 0 < r < R_1 \\ BJ_m(n_2 k_0 r) + CN_m(n_2 k_0 r) & R_1 < r < R_2 \\ DH_m^{(1)}(n_3 k_0 r) & R_2 < r < \infty \end{cases} \quad (44)$$

where n_1, n_2 , and n_3 are the refractive indices of the liquid core region, the silica micro-tube region and the outside air region, k_0 is the wave-vector in the vacuum; $J_m(\mathrm{n}k_0 r)$, $N_m(\mathrm{n}k_0 r)$ and $H_m^{(1)}(\mathrm{n}k_0 r)$ are respectively the m th order cylindrical Bessel function, Neumann function and Hankel function of the first kind. By matching the boundary conditions at the liquid/PMMA and PMMA/air interfaces, we obtain the eigen function equation, which can be used to calculate the resonance wavelength. The TE mode resonance with azimuthal number m is determined by

$$\frac{n_1 J_m(n_1 k_0 R_1)}{n_2 J'_m(n_1 k_0 R_1)} = \frac{(B/C) J_m(n_2 k_0 R_1) + N_m(n_2 k_0 R_1)}{(B/C) J'_m(n_2 k_0 R_1) + N'_m(n_2 k_0 R_1)} \quad (45)$$

$$\frac{B}{C} = \frac{n_3 H_m^{(1)}(n_3 k_0 R_2)\, N_m(n_2 k_0 R_2) - n_2 H_m^{(1)}(n_3 k_0 R_2)\, N_m(n_2 k_0 R_2)}{n_2 H_m^{(1)'}(n_3 k_0 R_2)\, J_m(n_2 k_0 R_2) - n_3 H_m^{(1)}(n_3 k_0 R_2)\, J'_m(n_2 k_0 R_2)} \quad (46)$$

For a given m number, there are a series of k_0 satisfying equations (57), which are referred to as the ϑth (n = 1, 2, 3, ...) order resonance mode. The radial and tangential components of the electrical field in the TE mode can be expressed in terms of Hz as

$$E_z = -\frac{m}{\omega \varepsilon_0 \varepsilon_r r} H_z \quad (47)$$

$$E_\varphi = -\frac{m}{i\omega \varepsilon_0 \varepsilon_r} \frac{\partial}{\partial z} H_z \quad (48)$$

2.3.3 Results

In the analysis, the following are the parameters for the micro-tube and its environment: inner radius R1=85 μm, outer radius R2=146.2 μm, and the refractive index of the PMMA as 1.4816 at 1.064 μm laser wavelength. Hollow tube has been considered to be filled with water.

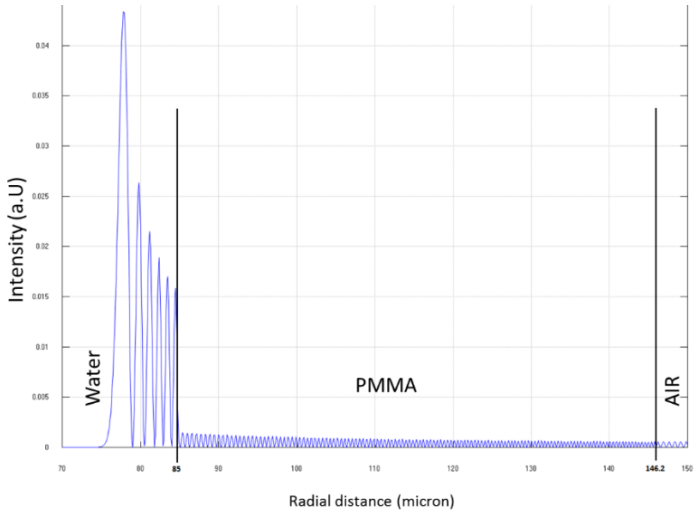

Figure 2-22: Radial electrical field intensity distribution for the resonance mode Er_{600} in OFRR

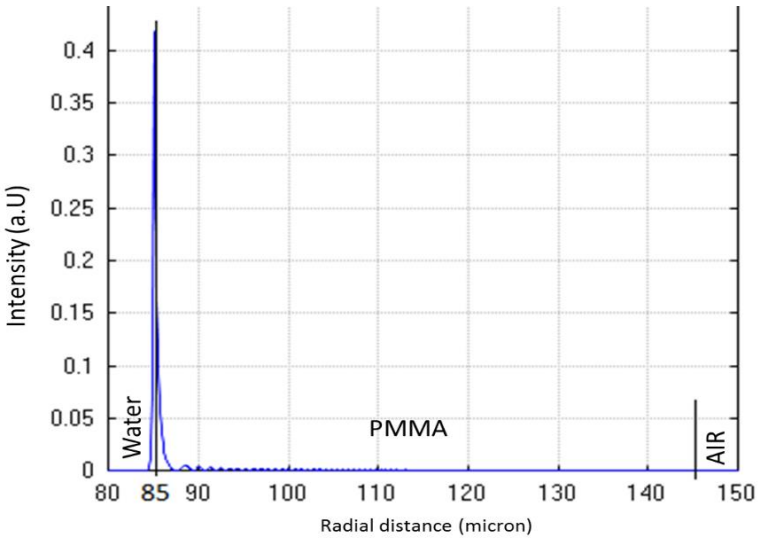

Figure 2-23: Radial electrical field intensity distribution for the resonance mode Er_{760}

The electrical field is primarily responsible for the resonance wavelength shift due to the refractive index change in the liquid. In the OFRR the radial electrical field of TE mode is much larger than the angular electrical field, thus it is important to focus on the radial electrical field (Er) distribution in the PMMA micro-tube. Figure 2-21 and 2-22 show the electric field distribution of TE mode with an azimuthal number of 600 and 760. It can be clearly seen that unlike typical mode the electric field in Figure 2-22 will be preferred as it has a higher electric field and resides at the boundary interface between the water and PMMA enabling the sensing of the interaction of glucose with VPBA and becoming sensitive to surface event.

2.4 Conclusion

Mathematical modelling and simulations were conducted on different fibre optics sensing methods. The objective of selecting a fibre structure for maximizing evanescent power fraction is achieved through the use of hollow core optical fibre as microresonator. This approach definitely poses advantages over other methods in terms of the possibility of miniaturisation of device and tunability of probing electric field. The Matlab code used for this analysis is provided in the Appendix.

Chapter 3 - Fabrication of VPBA doped polymer optical fibre

3.1 Investigation into the reversible covalent bond of boronic acid for glucose sensing

This study discusses the study of a boronic acid moiety which is known to bind with diols to form cyclic boronate esters. In spite of the high stability of covalent bonds thus formed, under certain conditions and in the presence of external stimuli the process is reversible thus aiding the development of continuous blood glucose monitoring. Different substituents have a significant effect on boronic acid. An electron-withdrawing group (EWG) decreases the pKa while electron donating groups (EDG) will increase the same. Hence different substitution can be used to tailor the properties of a boronic acid.

3.1.1 Theory

The internal charge transfer mechanism caused due to the binding of glucose to 4-vinylphenylboronic acid is responsible for the fluorescence quenching resulting in the signalling process.

Equilibrium of boronic acid in water is shown below. For stable binding, tetrahedral/dissociated form is preferred due to the stabilization of the structure by bond relaxation from 120^0 to 109^0 [42].

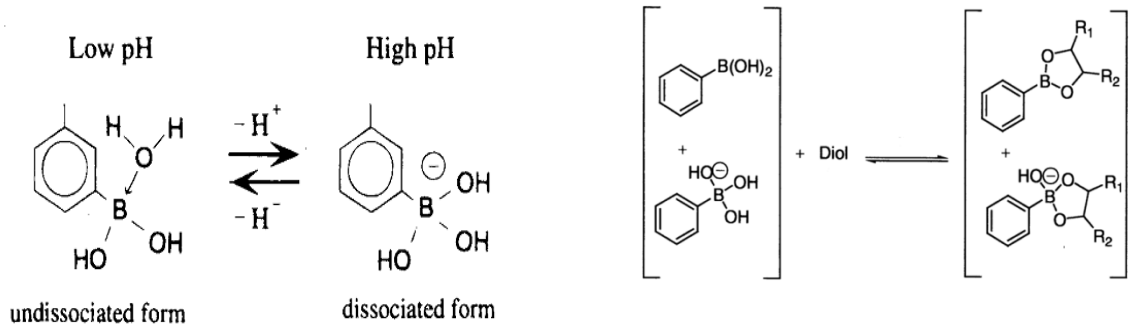

Figure 3-1: Equilibrium of boronic acid in water[42]

3.1.2 Materials & method

4-vinylphenylboronic acid (VPBA) was used as a boronic acid moiety. VPBA solution was made at a concentration of 250 μM in pH 7.3 phosphate buffer solution. Titration method was then used to vary glucose concentration from 0 to 200 mM. The interaction of VPBA with glucose was then characterised using UV/Vis/NIR spectrometer (Jasco V-570) and fluorescence spectrometer (Varian Cary).

3.1.3 UV-Visible absorption spectrum & fluorescence spectrum

The baseline correction is done with cuvettes filled with VPBA in phosphate buffer solution. The negative peak shown in Figure 3-2(a) is due to the reduction in absorbance at 274nm peak with increase in glucose concentration when compared with baseline correction.

3.1.3.a Absorption spectrum

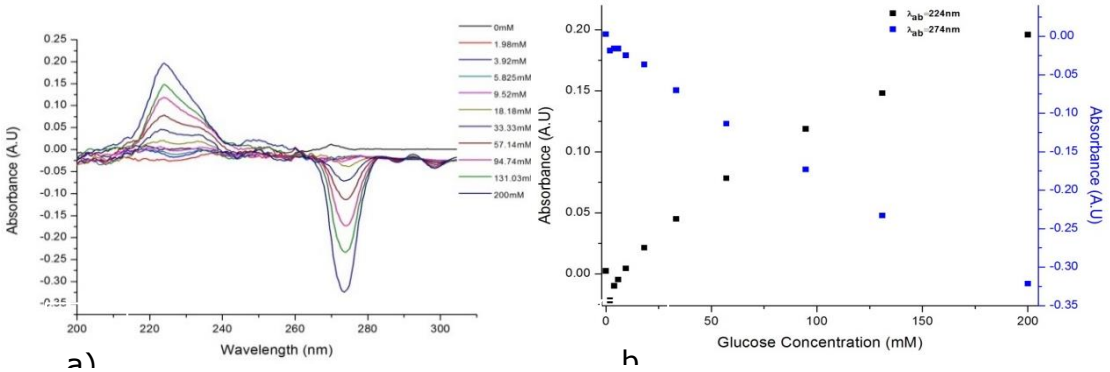

Figure 3-2: (a) Shows changes in absorption spectra upon varying glucose concentration from 0 to 200 mM. (b) Calibration curve showing the relation between absorption and glucose concentration. (λab = 224 nm, 274 nm)

3.1.3.b Fluorescence spectrum

Due to the instability of UV source at 224 nm only absorption at 274 nm was used for checking fluorescence.

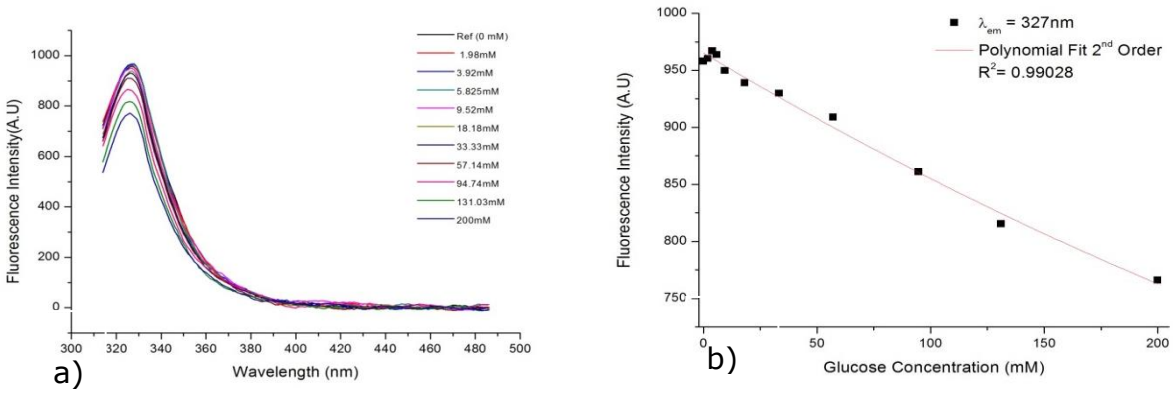

Figure 3-3: (a) Shows changes in emission spectra upon varying glucose concentration from 0 to 200 mM. (b) Calibration curve showing the relation between emission intensity and glucose concentration. (λex = 280 nm)

3.1.4 Results & discussion

Boronic acid derivatives have been identified as a suitable reagent due to their high affinity for glucose and their capability to form reversible complexes at physiological pH of 7.3. The study above suggests the importance of boronic

acid for the synthesis of a reusable sensor. Both fluorescence and absorption based sensing approaches can be implemented for sensor design.

3.2 A preliminary investigation into immobilisation of 4-vinylphenylboronic acid in PMMA matrix

As already discussed, among the methods used for detecting glucose, fluorescence detection methods are more versatile due to their high sensitivity. One of the methods is based on boronic acids derivatives. They are preferred here as they are known to bind with 1, 2 or 1, 3 diols with high affinity [94].

4-vinylphenylboronic acid (VPBA) has been used as a fluorophore for the study. The main objectives of the study here are to check the response of VPBA to glucose when attached to the PMMA matrix and whether it can be reused. This is important because in order to use VPBA with fibre structures proposed in chapter 2 the reagent should be active when doped in PMMA. To my knowledge from literature review, VPBA has never been used with PMMA matrix making this experiment novel [95], [96].

3.2.1 Materials

PMMA pellets, 4-vinylphenylboronic acid, anisole and D-glucose were purchased from Sigma - Aldrich and used in the experiment without any further purification.

3.2.2 Method

PMMA pellets were dissolved in solvent anisole at a concentration of 1 mg /ml by ultra-sonication. A 300 ppm concentration of VPBA in PMMA-Anisole solution was prepared. A thin layer of PMMA-VPBA layer was formed on the surface of glass by spin coating at 500 rpm (speciality coating systems-6800

series) and allowed for drying. Since the glucose detection range previously reported for VPBA in a polymer matrix of HEMA (hydroxyethylmethacrylate) in [42] is from $2.78x10^{-4}$ – $5.56x10^{-3}$ mM, glucose solution required for testing were made at a concentration of $2.8x10^{-4}$ mM in pH 7 phosphate buffer solution.

3.2.3 Experiment

The fluorescence spectrum of VPBA doped PMMA coated samples were taken using Perkin Elmer (LS-50B) fluorescence spectrometer. Emission peak was observed at 423 nm when excited at 228 nm with a slit width of 2.5 nm.

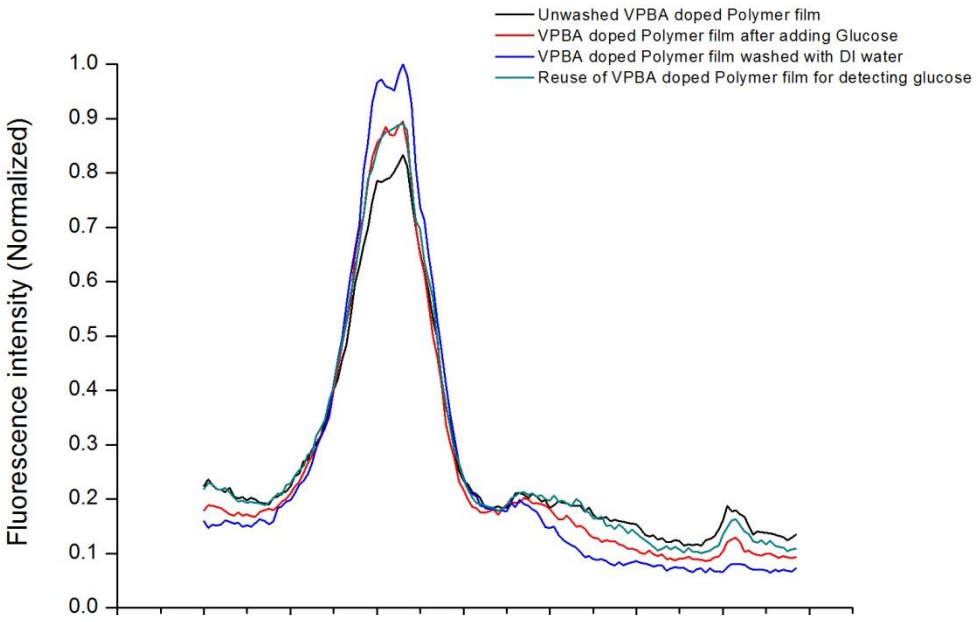

Figure 3-4: Change in emission spectrum upon adding glucose

λex = 228nm & λem = 423nm

Experiments were carried out in the order given below emission spectrum of the VPBA-PMMA polymer coating was taken and the values are shown by black curve. Glucose was added and an increase in spectral response was obtained, (red curve).

In order to check its regenerative capability, the thin layer was washed with de-ionized water. Here the fluorescence signal further increased, which can be explained as a result of washing leading to the change in the thin film surface.

Glucose was added for the second time. In both cases when glucose was added it can be seen that the resultant emission curves (red & green) were following each other, which is a good sign of stability in fluorescence signal upon adding glucose.

3.2.4 Results

The experiment thus confirms the diol sensing capability of VPBA in PMMA matrix and shows its regenerative capacity. Further increase in sensitivity can be achieved if the absorption of probing signal (at λ_{ex} = 228 nm) by PMMA could be avoided. It's a known fact that PMMA has heavy absorption for wavelength below 430 nm [80]. However, the use of far UV wavelength can be avoided by taking advantage of the conformal changes happening to VPBA moiety upon binding to glucose. This conformal change can be detected using a looped waveguide acting as a resonator. Apart from inherent high sensitivity, the use of resonator enables us to select the probing wavelength independent of VPBA's absorption spectrum. This hence will solve the problems associated with the use of PMMA.

3.3 Fabrication & characterisation of VPBA doped polymer optical fibre

3.3.1 Methyl methacrylate (MMA) purification

3.3.1.a) Removal of inhibitors

Methyl Methacrylate (MMA) is the precursor required for PMMA or Poly (methyl methacrylate). Commercial MMA is transported with polymerisation inhibitors which avoid polymerisation of MMA while in transport or during storage.

Inhibitor and any other dissolved impurities in MMA can be removed by washing it with a mixture of NaOH & water in 1:1 ratio. Any residue of NaOH can be then removed by further washing it with distilled water. In order to remove the water content from the MMA dehydrating agent ($CaCl_2$) is added and kept overnight.

3.3.1.b) Removal of low and high-density impurities

After this procedure, the MMA needs to be filtered through filter paper and undergoes further purification by distillation. After distillation, MMA is free of any inhibitors or impurities and is ready for polymerization.

3.3.2 Polymerisation of MMA

Polymerisation process starts by adding a measured quantity (0.4 wt. %) of initiator (benzoyl peroxide (BPO)). In order to keep the length of a polymer chain within useful limits, a chain transfer agent (0.1 wt. %) n-butyl mercaptan is added. The solution is then poured into glass tubes. The tubes are then kept in an oil bath (70^0C) for 72 hours for polymerisation. The preform tube thus obtained is drawn into a fibre using a fibre drawing station at 180^0C.

Preform to fibre diameter ratio is governed by the equation as given below

$$\frac{D^2}{d^2} = \frac{v_{draw}}{v_{preform}} \quad (49)$$

D = Preform diameter, d = Fibre diameter, v_{draw} = Fibre draw speed,

$v_{preform}$ = Preform feed rate

Draw Conditions

		HC-POF(VPBA)	HC-PCF(VPBA+Rh-6G)
Draw Rate (µm/s)		20000	20000
Feed rate (µm/s)		5	5
Temp. ^{0}C		180	190
Preform Diameter (mm)	Inner (mm)	6.2	6.2
	Outer (mm)	13.12	13.12

3.3.3 Immobilization of VPBA & Rhodamine 6G into PMMA matrix

3.3.3.a) VPBA Alone

Immobilization of VPBA on to a polymer matrix is inevitable for sensor design. Preliminary studies and literature support immobilization of VPBA onto PMMA. VPBA was added at a concentration of 500 µM to MMA before polymerisation.

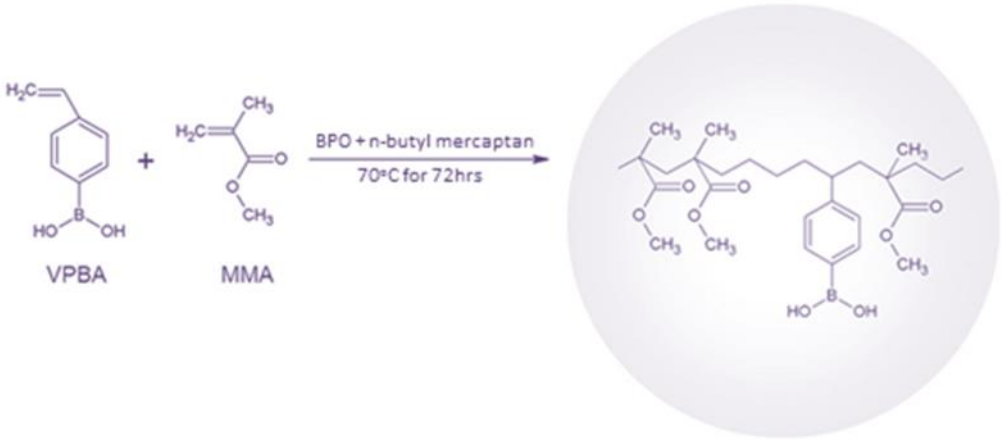

Figure 3-5: Immobilization of VPBA [97]

3.3.3.b) VPBA and Rhodamine 6G

Rhodamine 6G is a highly fluorescent dye having remarkably high photostability and fluorescent quantum yield (0.95). It can also be used as laser dye or as the gain medium in dye lasers. Fluorescence excitation is at 530 nm with an emission range 555 to 585 nm with a peak at 566 nm, in solvents. Addition of Rh-6G to MMA will convert the preform to gain media where lasing can take place. Hollow fibre drawn from the preform is capable of sustaining whispering gallery modes whose properties are highly sensitive to the surrounding environment. VPBA and Rh-6G were added at a concentration 500 µM and 250 µM respectively to MMA.

3.3.4 Fabrication of the specialized fibre structure

3.3.4.a) Hollow Core Polymer Optical Fibre

In addition to the steps described in section 3.3.2, in order to introduce a hollow core, a Teflon rod is inserted into the glass tube vessel (as shown in the figure below, 3-6) so that hollow core preform will be obtained after

polymerisation. Figure 3-7 shows typical preforms made for drawing fibres, with Rh-6G doped preform (A) which is clearly differentiable resulting from its absorption & emission bands in the visible region. Transparency of VPBA and PMMA are retained in the other preforms (B&C) even after the solidification/polymerisation phase. Figures 3-8 & 3-9 show pictures of fibres drawn, with Fig. 3-8 showing a clear indication of Rh-6G doping.

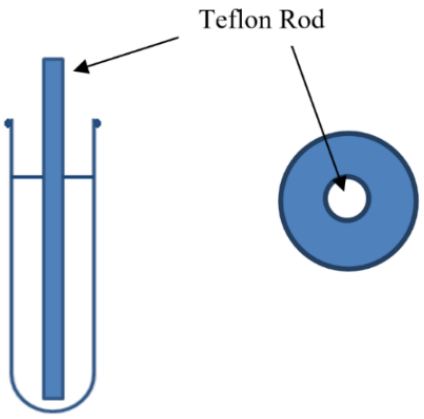

Figure 3-6: Creating a central hole in PMMA preform

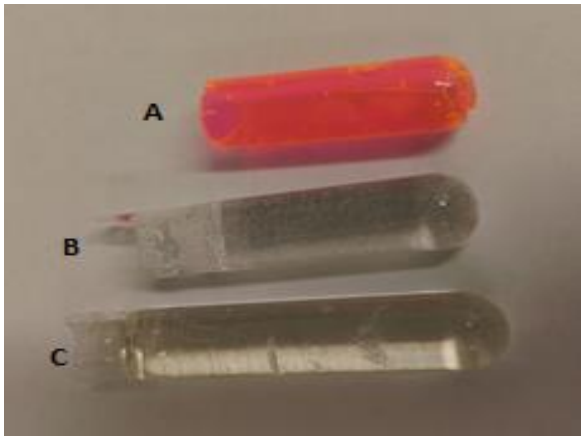

Figure 3-7: PMMA preforms A) With Rh-6G and VPBA, B) & C) with only VPBA

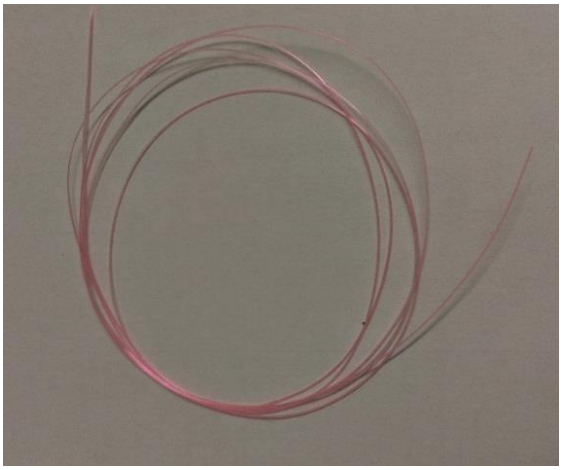

Figure 3-8: Fabricated HC-POF with Rh-6G & VPBA

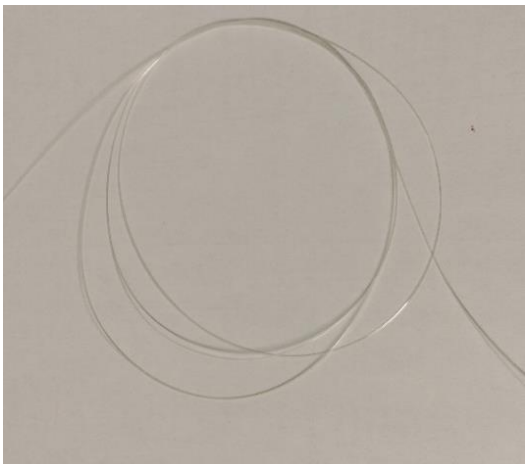

Figure 3-9: Fabricated HC-POF with only VPBA

3.3.5 Characterisation of fabricated VPBA doped POF, HC-POF & MSF

3.3.5.a) Structural analysis using Scanning Electron Microscope (SEM)

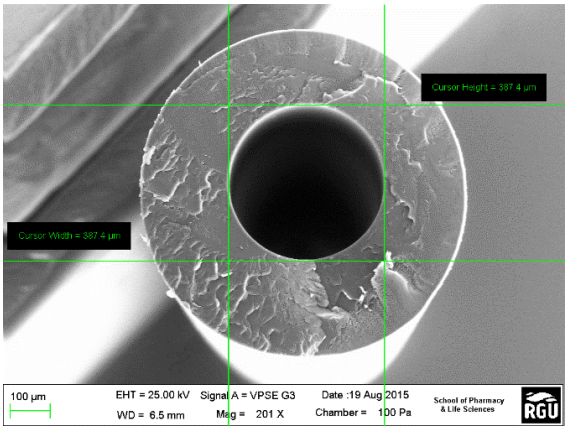

Figure 3-10: HC-POF doped with VPBA, hole dia = 387.4 µm

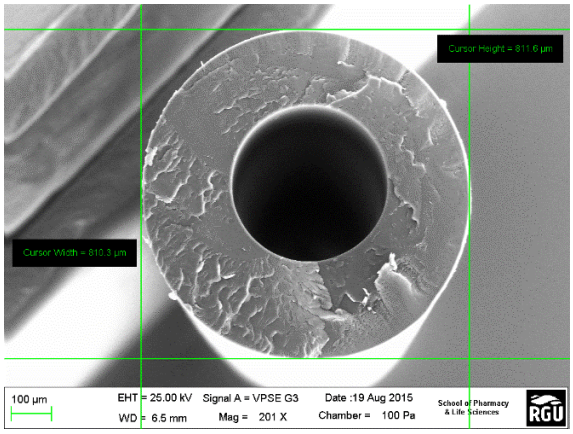

Figure 3-11: HC-POF doped with VPBA, fibre dia = 810.3 µm

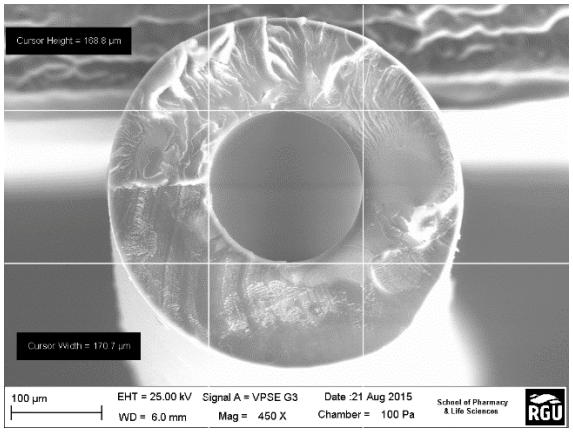

Figure 3-12: HC-POF doped with VPBA and Rh-6G, hole dia = 169.75 µm

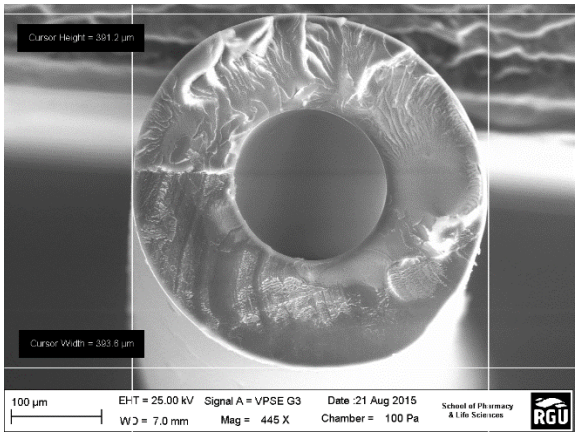

Figure 3-13: HC-POF doped with VPBA and Rh-6G, fibre dia = 392.4 µm

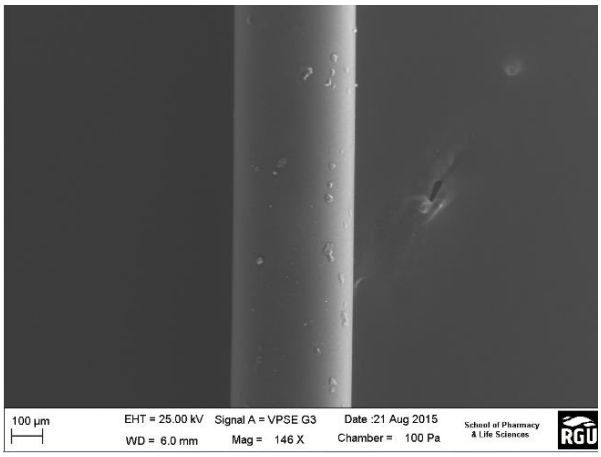

Figure 3-14: Side view for the HC-POF doped with VPBA and Rh-6G, fibre dia = 392.4 µm

Above figures 3-10 to 3-14 show structural details of fabricated HC-POF when seen through SEM. Figure 3-10 and 3-11 show the cross-section of the two fabricated fibres with VPBA doping. The central part as discussed before is hollow and has been maintained even after the hollow preform has been extruded to thin fibre. The fibre end has been cut with a general cutter hence the marks on the end. The fibre maintains approximately 0.43~0.48 hole size to total fibre size ratio. The higher ratio has been avoided so as to maintain

the structural integrity of the fibre by not allowing the central hole to collapse. Figure 3-14 shows the surface features present on the side of the fabricated fibre. The figure clearly shows the surface to be smooth. A smooth surface helps in minimizing the scattering of probing field and thereby reduce losses.

3.3.5.b) Fluorescence emission spectrum for Rh-6G and VPBA doped hollow fibre.

To confirm the fluorescence emission properties of the Rh-6G in the doped fibre, it's emission was tested with the help of a green LED. On illumination with the green LED, the fibre produced a reddish glow indicating its fluorescence properties even after doping and drawing. Further, the glow was clearly visible throughout the fibre confirming the light guiding properties of the fibre.

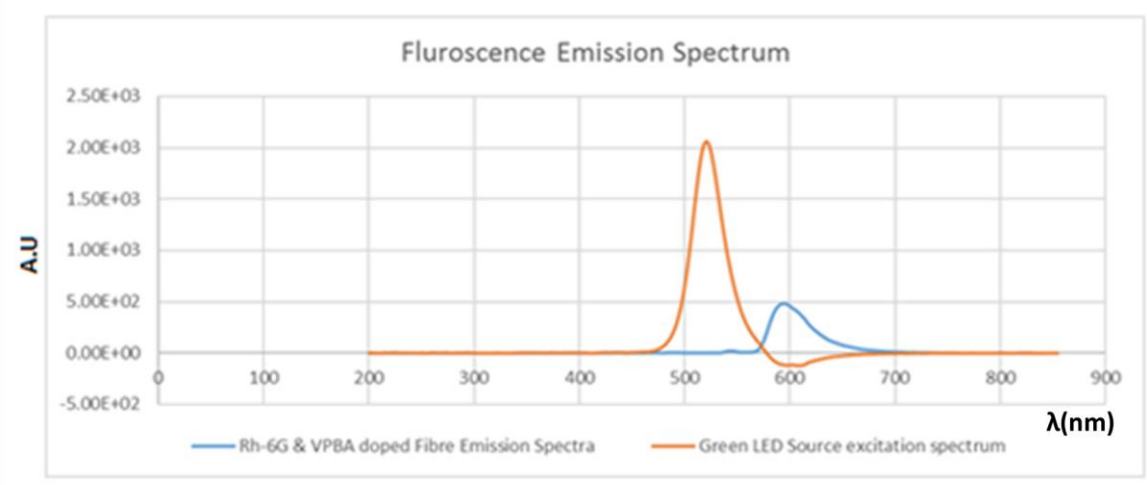

Figure 3-15: Fluorescence emission spectrum for Rh-6G and VPBA doped HC-POF

The figure 3-15 shows excitation spectrum of the green LED (in red) with a peak around 530 nm and corresponding emission from the fibre peaking around 591 nm (in blue), in line with Ali et.al, [98]. The LED emission was

allowed to fall on the HCPOF and the fluorescence was collected from the fibre using Stellarnet-2000 UV-Vis spectrometer.

3.3.6 Conclusion

VPBA has been identified as a new moiety which can be immobilized into PMMA and at the same time used for glucose sensing. The proposed fibre structure in Chapter 2 has been realized and the SEM image confirm the same. Rh-6G has been also successfully immobilized with VPBA and is active. The said configuration can be helpful to create microresonator with the lasing gain medium as described in section 3.3.3.b. From the SEM images, it is clear that fabricated HC-POF is of good quality. Further, the Rh-6G has retained its fluorescence properties even after doping with PMMA & VPBA and fibre drawing process.

Chapter 4 - Conclusion and future work

In this study, a novel minimally invasive method to detect glucose in the interstitial fluid based on an optofluidic ring resonator (OFRR) has been proposed. The proposed OFRR also integrates extraction and delivery of interstitial fluid, and subsequent glucose sensing with a simple PMMA capillary which is biocompatible and can be mass produced.

Primary investigation supports the novelty of proposed sensor in terms of design, functionality, sensitivity and selectivity. Mathematical simulations have confirmed the increase in evanescent field fraction, interaction volume and direct field interaction in MSF, ITF and OFRR. PMMA has been used as fibre material for better biocompatibility. Boronic acid derivatives have been identified as reagents due to their high affinity for glucose and their capability to form reversible complexes at physiological pH of 7.4. Boronic acid is also effective when immobilized in PMMA matrix for better sensor stability and reusability. The usability of this configuration has been analysed in Chapter 2 section 2.3 and been found promising. However, the same needs to be checked in-vitro for varying levels of glucose concentration. The new approach should be tested against all possibilities of biocompatibility issues, interference from other blood constituents. In future polymer optical fibres (POFs) are favoured for the low cost and simplicity of the manufacturing process.

PMMA based OFRR definitely suffer from loss due to surface sidewall scattering loss, bending radiation loss etc. This considerably worsens the performance by widening the filter bandwidth, reduction in finesse. To compensate such losses a PMMA - OFRR with gain media can be used [44] causing a significant rise in

gain and hence the Q-factor and sensitivity. The same has been fabricated in this study.

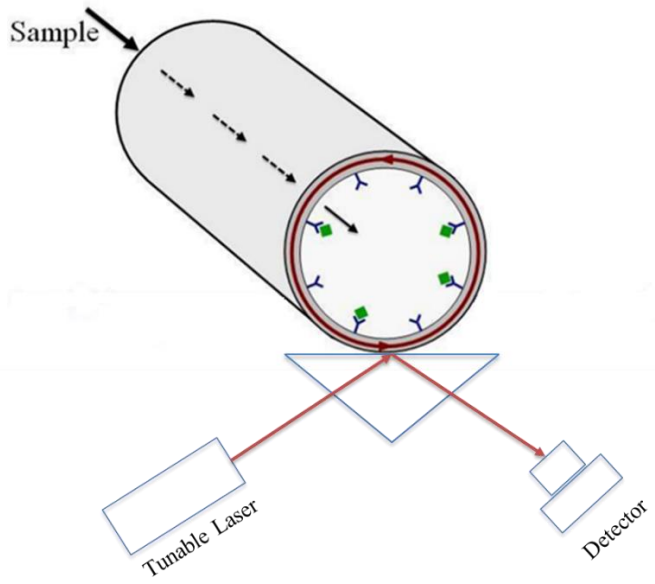

Figure 4-1: Representation of proposed sensor

Figure 4-1 shows a representation of proposed sensor configuration in which the need for complex optical spectrum analysers can be avoided by using a laser diode or LED with a photo detector which can probe the shift in resonance vs glucose concentration.

References

[1] Alberti, Kurt George Matthew Mayer and P. Zimmet, "Definition, diagnosis and classification of diabetes mellitus and its complications. Part 1: diagnosis and classification of diabetes mellitus. Provisional report of a WHO consultation," *Diabetic Med.,* vol. 15, *(7),* pp. 539-553, 1998.

[2] J. E. Shaw, R. A. Sicree and P. Z. Zimmet, "Global estimates of the prevalence of diabetes for 2010 and 2030," *Diabetes Res. Clin. Pract.,* vol. 87, *(1),* pp. 4-14, 1, 2010.

[3] I. Diabetes Atlas, "IDF DIABETES ATLAS Sixth edition," vol. 2014, *(10/08),* 2013.

[4] S. K. Vashist *et al*, "Technology behind commercial devices for blood glucose monitoring in diabetes management: a review," *Anal. Chim. Acta,* vol. 703, *(2),* pp. 124-136, 2011.

[5] D. Daneman, "Type 1 diabetes," *The Lancet,* vol. 367, *(9513),* pp. 847-858, 3/11–17, 2006.

[6] M. Stumvoll, B. J. Goldstein and T. W. van Haeften, "Type 2 diabetes: principles of pathogenesis and therapy," *The Lancet,* vol. 365, *(9467),* pp. 1333-1346, 4/9–15, 2005.

[7] B. E. Metzger, "Summary and recommendations of the third international workshop-conference on gestational diabetes mellitus," *Diabetes,* vol. 40, *(Supplement 2),* pp. 197-201, 1991.

[8] D. M. Nathan, "Long-term complications of diabetes mellitus," *N. Engl. J. Med.,* vol. 328, *(23),* pp. 1676-1685, 1993.

[9] D. S. Fong *et al*, "Retinopathy in diabetes," *Diabetes Care,* vol. 27, *(suppl 1),* pp. s84-s87, 2004.

[10] B. Isomaa *et al*, "Cardiovascular morbidity and mortality associated with the metabolic syndrome," *Diabetes Care,* vol. 24, *(4),* pp. 683-689, 2001.

[11] J. J. Duby *et al*, "Diabetic neuropathy: an intensive review," *American Journal of Health-System Pharmacy,* vol. 61, *(2),* pp. 160-173, 2004.

[12] S. P. O'Brien, M. Schwedler and M. D. Kerstein, "Peripheral neuropathies in diabetes," *Surg. Clin. North Am.,* vol. 78, *(3),* pp. 393-408, 1998.

[13] M. E. Molitch *et al*, "Nephropathy in diabetes," *Diabetes Care,* vol. 27 Suppl 1, pp. S79-83, Jan, 2004.

[14] H. Shamoon, H. Duffy, N. Fleischer, S. Engel, "The Effect of Intensive Treatment of Diabetes on the Development and Progression of Long-Term

Complications in Insulin-Dependent Diabetes Mellitus," *N. Engl. J. Med.,* vol. 329, *(14),* pp. 977-986, 09/30; 2014/02, 1993.

[15] Anonymous "Diabetes Mellitus: Report of a WHO Study Group," *World Health Organisation,* vol. Technical; Report Series, *(727),* 1985.

[16] B. Leese, "Prevention of diabetes mellitus. Report of a WHO Study Group. WHO technical report series 844, Geneva, 1994. No. of pages: 100. ISBN 92 4 120844 9," *Health Econ.,* vol. 4, *(4),* pp. 331-332, 1995.

[17] B. H. Esteridge, A. P. Reynolds and N. J. Walters, "Basic medical laboratory techniques," in Anonymous Cengage Learning, 2000, pp. 430-431.

[18] J. Wang, "Electrochemical glucose biosensors," *Chem. Rev.,* vol. 108, *(2),* pp. 814-825, 2008.

[19] M. A. Arnold and G. W. Small, "Noninvasive glucose sensing," *Anal. Chem.,* vol. 77, *(17),* pp. 5429-5439, 2005.

[20] O. S. Khalil, "Non-invasive glucose measurement technologies: an update from 1999 to the dawn of the new millennium," *Diabetes Technology & Therapeutics,* vol. 6, *(5),* pp. 660-697, 2004.

[21] N. Oliver *et al*, "Glucose sensors: a review of current and emerging technology," *Diabetic Med.,* vol. 26, *(3),* pp. 197-210, 2009.

[22] J. Shao *et al*, "In Vivo Blood Glucose Quantification Using Raman Spectroscopy," *PloS One,* vol. 7, *(10),* pp. e48127, 2012.

[23] L. G. Anderson, *Raman Spectroscopy*,2000

[24] D. I. Ellis and R. Goodacre, "Metabolic fingerprinting in disease diagnosis: biomedical applications of infrared and Raman spectroscopy," *Analyst,* vol. 131, *(8),* pp. 875-885, 2006.

[25] V. V. Sapozhnikova *et al*, "Effect on blood glucose monitoring of skin pressure exerted by an optical coherence tomography probe," *J. Biomed. Opt.,* vol. 13, *(2),* pp. 021112-021112-4, 2008.

[26] Y. Fujimoto, "CLEO: 2011 Baltimore ④ Plenary Session," .

[27] R. T. Kurnik *et al*, "Application of the mixtures of experts algorithm for signal processing in a noninvasive glucose monitoring system," *Sensors Actuators B: Chem.,* vol. 60, *(1),* pp. 19-26, 1999.

[28] V. L. Alexeev *et al*, "Photonic crystal glucose-sensing material for noninvasive monitoring of glucose in tear fluid," *Clin. Chem.,* vol. 50, *(12),* pp. 2353-2360, 2004.

[29] R. Badugu, J. R. Lakowicz and C. D. Geddes, "A glucose sensing contact lens: a non-invasive technique for continuous physiological glucose monitoring," *J. Fluoresc.,* vol. 13, *(5),* pp. 371-374, 2003.

[30] M. Yamaguchi, M. Mitsumori and Y. Kano, "Noninvasively measuring blood glucose using saliva," *Engineering in Medicine and Biology Magazine, IEEE,* vol. 17, *(3),* pp. 59-63, 1998.

[31] J. Hönes, P. Müller and N. Surridge, "The technology behind glucose meters: test strips," *Diabetes Technology & Therapeutics,* vol. 10, *(S1),* pp. S-10-S-26, 2008.

[32] E. Wilkins and P. Atanasov, "Glucose monitoring: state of the art and future possibilities," *Med. Eng. Phys.,* vol. 18, *(4),* pp. 273-288, 1996.

[33] J. Hönes, P. Müller and N. Surridge, "The technology behind glucose meters: test strips," *Diabetes Technology & Therapeutics,* vol. 10, *(S1),* pp. S-10-S-26, 2008.

[34] S. Churchouse *et al*, "Needle enzyme electrodes for biological studies," *Biosensors,* vol. 2, *(6),* pp. 325-342, 1986.

[35] E. Kulcu *et al*, "Physiological differences between interstitial glucose and blood glucose measured in human subjects," *Diabetes Care,* vol. 26, *(8),* pp. 2405-2409, Aug, 2003.

[36] Y. Wickramasinghe, Y. Yang and S. Spencer, "Current problems and potential techniques in in vivo glucose monitoring," *J. Fluoresc.,* vol. 14, *(5),* pp. 513-520, 2004.

[37] A. M. Corstjens *et al*, "Accuracy and feasibility of point-of-care and continuous blood glucose analysis in critically ill ICU patients," *Critical Care,* vol. 10, *(5),* pp. R135, 2006.

[38] J. Yan *et al*, "The relationship among pKa, pH, and binding constants in the interactions between boronic acids and diols—it is not as simple as it appears," *Tetrahedron,* vol. 60, *(49),* pp. 11205-11209, 2004.

[39] S. Choi, D. Chung and H. Kwen, "Fabrication of Biosensors Using Vinyl Polymer-grafted Carbon Nanotubes," *New Perspectives in Biosensors Technology and Applications,* pp. 245-268, 2011.

[40] S. Arimori, C. J. Ward and T. D. James, "A d-glucose selective fluorescent assay," *Tetrahedron Lett.,* vol. 43, *(2),* pp. 303-305, 2002.

[41] G. Springsteen and B. Wang, "A detailed examination of boronic acid–diol complexation," *Tetrahedron,* vol. 58, *(26),* pp. 5291-5300, 2002.

[42] D. G. Hall, *Structure, Properties, and Preparation of Boronic Acid Derivatives. Overview of their Reactions and Applications.* John Wiley & Sons: Weinheim, Germany, 2006.

[43] S. Çubuk *et al*, "Development of photopolymerized fluorescence sensor for glucose analysis," *Sensors Actuators B: Chem.,* vol. 181, pp. 187-193, 2013.

[44] H. Chen, "Theoretical analysis of active ring microresonator filter," in *Integrated Optoelectronic Devices 2007,* 2007, pp. 64750K-64750K-6.

[45] V. Bhatia and A. M. Vengsarkar, "Optical fiber long-period grating sensors," *Opt. Lett.,* vol. 21, *(9),* pp. 692-694, 1996.

[46] A. Iadicicco *et al*, "Thinned fiber Bragg gratings as high sensitivity refractive index sensor," *Photonics Technology Letters, IEEE,* vol. 16, *(4),* pp. 1149-1151, 2004.

[47] C. Dafu *et al*, "Optical-fibre pH sensor," *Sensors Actuators B: Chem.,* vol. 12, *(1),* pp. 29-32, 1993.

[48] J. F. Alder, "Optical fibre chemical sensors," *Fresenius' Zeitschrift Für Analytische Chemie,* vol. 324, *(5),* pp. 372-375, 1986.

[49] M. van Eijkelenborg, "Imaging with microstructured polymer fibre," *Optics Express,* vol. 12, *(2),* pp. 342-346, 2004.

[50] K. Grattan and T. Sun, "Fiber optic sensor technology: an overview," *Sensors and Actuators A: Physical,* vol. 82, *(1),* pp. 40-61, 2000.

[51] R. K. Shevgaonkar, "Advanced Optical Communication," *Nptel,* vol. 2014, *(09/10),* 2014.

[52] E. S. Bahaa and C. T. Malvin, "Fundamentals of photonics," *New York/A WILEY-INTERSCIENCE PUBLICATION,* 1991.

[53] G. Keiser, *Optical Fiber Communications.* Wiley Online Library, 2003.

[54] D. Axelrod, J. C. Long and M. W. Davidson, "Evanescent field polarization and intensity profiles," vol. 2014, *(08/10),* .

[55] M. Ahmad and L. L. Hench, "Effect of taper geometries and launch angle on evanescent wave penetration depth in optical fibers," *Biosensors and Bioelectronics,* vol. 20, *(7),* pp. 1312-1319, 1/15, 2005.

[56] Y. Wu *et al*, "Less-mode optic fiber evanescent wave absorbing sensor: Parameter design for high sensitivity liquid detection," *Sensors Actuators B: Chem.,* vol. 122, *(1),* pp. 127-133, 3/8, 2007.

[57] G. D, "Weakly guiding fibers," *Appl.Opt,* vol. 10, pp. 2252-2258, 1971.

[58] C. R. Taitt, G. P. Anderson and F. S. Ligler, "Evanescent wave fluorescence biosensors," *Biosensors and Bioelectronics,* vol. 20, *(12),* pp. 2470-2487, 6/15, 2005.

[59] V. Ruddy, B. MacCraith and J. Murphy, "Evanescent wave absorption spectroscopy using multimode fibers," *J. Appl. Phys.,* vol. 67, *(10),* pp. 6070-6074, 1990.

[60] A. W. Snyder and J. Love, *Optical Waveguide Theory.* Springer, 1983*190*.

[61] G. Keiser, *Optical Fiber Communications.* Wiley Online Library, 2003.

[62] C. S. Burke *et al*, "Planar optical sensors and evanescent wave effects," in *Optical Chemical Sensors*Anonymous Springer, 2006, pp. 193-215.

[63] R. T. Schermer and J. H. Cole, "Improved bend loss formula verified for optical fiber by simulation and experiment," *Quantum Electronics, IEEE Journal Of,* vol. 43, *(10),* pp. 899-909, 2007.

[64] B. Eggleton *et al*, "Microstructured optical fiber devices," *Optics Express,* vol. 9, *(13),* pp. 698-713, 2001.

[65] S. O. Konorov *et al*, "Hollow-core photonic crystal fiber-optic probes for Raman spectroscopy," *Opt. Lett.,* vol. 31, *(12),* pp. 1911-1913, 2006.

[66] J. Ma and W. Bock, "Modeling of photonic crystal fiber with air holes sealed at the fiber end and its application to fluorescent light collection efficiency enhancement," *Optics Express,* vol. 13, *(7),* pp. 2385-2393, 2005.

[67] T. M. Monro *et al*, "Sensing with microstructured optical fibres," *Measurement Science and Technology,* vol. 12, *(7),* pp. 854, 2001.

[68] R. B. Thompson, "Fluorescence-based fiber-optic sensors," in *Topics in Fluorescence Spectroscopy*Anonymous Springer, 2002, pp. 345-365.

[69] J. Knight *et al*, "All-silica single-mode optical fiber with photonic crystal cladding," *Opt. Lett.,* vol. 21, *(19),* pp. 1547-1549, 1996.

[70] T. M. Monro and D. J. Richardson, "Holey optical fibres: Fundamental properties and device applications," *Comptes Rendus Physique,* vol. 4, *(1),* pp. 175-186, 2003.

[71] I. Thorlabs, "Hollow Core Photonic Crystal Fibers ," vol. 2014, 2014.

[72] S. Li and K. Ng, "Monte Carlo study of the sphere packing problem," *Physica A: Statistical Mechanics and its Applications,* vol. 321, *(1),* pp. 359-363, 2003.

[73] H. Ho *et al*, "Optimizing microstructured optical fibers for evanescent wave gas sensing," *Sensors Actuators B: Chem.,* vol. 122, *(1),* pp. 289-294, 2007.

[74] A. Cucinotta *et al*, "Holey fiber analysis through the finite-element method," *Photonics Technology Letters, IEEE,* vol. 14, *(11),* pp. 1530-1532, 2002.

[75] C. Schulze *et al*, "Mode resolved bend loss in few-mode optical fibers," *Optics Express,* vol. 21, *(3),* pp. 3170-3181, 2013.

[76] J. A. Howarter and J. P. Youngblood, "Optimization of silica silanization by 3-aminopropyltriethoxysilane," *Langmuir,* vol. 22, *(26),* pp. 11142-11147, 2006.

[77] J. Brzoska, I. B. Azouz and F. Rondelez, "Silanization of solid substrates: a step toward reproducibility," *Langmuir,* vol. 10, *(11),* pp. 4367-4373, 1994.

[78] J. H. Cramp, R. M. Mortier, R. T. Murray and R. F. Reid, "Fibre optic sensor with bonded dye," US 4560248 A, 1985.

[79] I. Malitson, "Interspecimen comparison of the refractive index of fused silica," *Josa,* vol. 55, *(10),* pp. 1205-1208, 1965.

[80] S. N. Kasarova *et al*, "Analysis of the dispersion of optical plastic materials," *Optical Materials,* vol. 29, *(11),* pp. 1481-1490, 7, 2007.

[81] G. M. Hale and M. R. Querry, "Optical constants of water in the 200-nm to 200-μm wavelength region," *Appl. Opt.,* vol. 12, *(3),* pp. 555-563, 1973.

[82] S. G. Johnson, "Notes on perfectly matched layers (PMLs)," *Lecture Notes, Massachusetts Institute of Technology, Massachusetts,* 2008.

[83] A. Taflove and S. C. Hagness, "Computationai Electrodynamics," 2000.

[84] M. Heiblum and J. H. Harris, "Analysis of curved optical waveguides by conformal transformation," *IEEE J. Quant. Electron.,* vol. 11, pp. 75-83, 1975.

[85] Y. L. Hoo *et al*, "Design and modeling of a photonic crystal fiber gas sensor," *Appl. Opt.,* vol. 42, *(18),* pp. 3509-3515, 2003.

[86] R. T. Schermer and J. H. Cole, "Improved bend loss formula verified for optical fiber by simulation and experiment," *Quantum Electronics, IEEE Journal Of,* vol. 43, *(10),* pp. 899-909, 2007.

[87] J. Peter *et al*, "Microring lasing from a dye-doped polymer-coated silica fiber," *Laser Physics,* vol. 23, *(11),* pp. 115104, 2013.

[88] J. C. Knight, "Photonic crystal fibres," *Nature,* vol. 424, *(6950),* pp. 847-851, 2003.

[89] P. Russell, "Photonic crystal fibers," *Science,* vol. 299, *(5605),* pp. 358-362, Jan 17, 2003.

[90] F. Cox, A. Argyros and M. Large, "Liquid-filled hollow core microstructured polymer optical fiber," *Optics Express,* vol. 14, *(9),* pp. 4135-4140, 2006.

[91] A. Dupuis *et al*, "Prospective for biodegradable microstructured optical fibers," *Opt. Lett.,* vol. 32, *(2),* pp. 109-111, 2007.

[92] W. Lukosz, "Integrated optical chemical and direct biochemical sensors," *Sensors Actuators B: Chem.,* vol. 29, *(1),* pp. 37-50, 1995.

[93] C. F. Bohren and D. R. Huffman, *Absorption and Scattering of Light by Small Particles.* Wiley New York, 1983*10*.

[94] J. C. Pickup *et al*, "Fluorescence-based glucose sensors," *Biosensors and Bioelectronics,* vol. 20, *(12),* pp. 2555-2565, 2005.

[95] S. Çubuka *et al*, "UV Cured Boronic Acid Based Fluorescence Sensor for the Determination of Glucose," *Chemical Engineering,* vol. 32, 2013.

[96] S. Çubuk *et al*, "Development of photopolymerized fluorescence sensor for glucose analysis," *Sensors Actuators B: Chem.,* vol. 181, pp. 187-193, 2013.

[97] H. Sakalak *et al*, "One-pot synthesis of biocompatible boronic acid-functionalized poly (methyl methacrylate) nanoparticles at sub-100 nm scale for glucose sensing," *Journal of Nanoparticle Research,* vol. 16, *(12),* pp. 2767, 2014.

[98] H. Ali, "Al-Hamdani, Rafa, H. Rajaa Nader." Study the spectral Properties of thin films of Rhodamine 6G dyes doped polymer (PMMA) dissolved in Chloroform," *Iraqi Journal of Physics,* vol. 12, *(23),* pp. 59-64, 2014.

[99] E.Marin, *Optical fiber sensors-Evanescent field*. *SCIRN - PRN University of Maine,2007*

Appendix - MATLAB code for simulation of OFRR

```
clear all;

close all;

clc;

% 2D- Plot

m = 600

n1 = 1.320;

n2 = 1.4816;

n3 = 1.0;

R1 = 85;

R2 = 146.2 ;

lam = 1.064;

k0 = 2*pi/lam;



J11 = besselj(m,k0*n1*R1);

J21 = besselj(m,k0*n2*R1);

J22 = besselj(m,k0*n2*R2);

Jd22 = (besselj(m-1,k0*n2*R2) - besselj(m+1,k0*n2*R2))/2;
```

```
H12 = besselh(m,k0*n1*R2);

H32 = besselh(m,k0*n3*R2);

Hd12 = (besselh(m-1,k0*n1*R2) - besselh(m+1,k0*n1*R2))/2;

Y21 = bessely(m,k0*n2*R1);

Y22 = bessely(m,k0*n2*R2);

Yd22 = (bessely(m-1,k0*n2*R2) - bessely(m+1,k0*n2*R2))/2;



C = (n2*H12*Yd22 - n3*Hd12*Y22)/(n3*Hd12*J22 - n2*H12*Jd22);



Am1 = (C*J21 + Y21)/J11;



Am3 = (C*J22 + Y22)/H32;



theta=0;



R = 0:0.1:1.2*R2;

for ii = 1:length(R)

   r= R(ii);
```

```
    if r < R2
        if r < R1
            Ez(ii)  = Am1*besselj(m,k0*n1*r)*exp(1i*m*theta);
        else Ez(ii) = (C*besselj(m,k0*n2*r) + bessely(m,k0*n2*r))*exp(1i*m*theta);

        end
    else Ez(ii) = Am3*besselh(m,k0*n3*r)*exp(1i*m*theta);
    end
end
Iz=real(Ez).^2;
plot(R,real(Iz));
grid
axis([70,150,0,.045],"square");
graphics_toolkit("gnuplot");
```